Biophysical *Journal*
Article

Biophysical Society

Infrared Excitation Induces Heating and Calcium Microdomain Hyperactivity in Cortical Astrocytes

Elke Schmidt[1] and Martin Oheim[1,*]
[1]Université de Paris, SPPIN - Saints-Pères Paris Institute for the Neurosciences, CNRS, Paris, France

ABSTRACT Unraveling how neural networks process and represent sensory information and how these cellular signals instruct behavioral output is a main goal in neuroscience. Two-photon activation of optogenetic actuators and calcium (Ca^{2+}) imaging with genetically encoded indicators allow, respectively, the all-optical stimulation and readout of activity from genetically identified cell populations. However, these techniques locally expose the brain to high near-infrared light doses, raising the concern of light-induced adverse effects on the biology under study. Combining 2P imaging of Ca^{2+} transients in GCaMP6f-expressing cortical astrocytes and unbiased machine-based event detection, we demonstrate the subtle build-up of aberrant microdomain Ca^{2+} transients in the fine astroglial processes that depended on the average rather than peak laser power. Illumination conditions routinely being used in biological 2P microscopy (920-nm excitation, ~100-fs, and ~10 mW average power) increased the frequency of microdomain Ca^{2+} events but left their amplitude, area, and duration largely unchanged. Ca^{2+} transients in the otherwise silent soma were secondary to this peripheral hyperactivity that occurred without overt morphological damage. Continuous-wave (nonpulsed) 920-nm illumination at the same average power was as damaging as femtosecond pulses, unraveling the dominance of a heating-mediated damage mechanism. In an astrocyte-specific inositol 3-phosphate receptor type-2 knockout mouse, near-infrared light-induced Ca^{2+} microdomains persisted in the small processes, underpinning their resemblance to physiological inositol 3-phosphate receptor type-2-independent Ca^{2+} signals, whereas somatic hyperactivity was abolished. We conclude that, contrary to what has generally been believed in the field, shorter pulses and lower average power can help to alleviate damage and allow for longer recording windows at 920 nm.

SIGNIFICANCE Imaging the fine structure and function of the brain has become possible with two-photon microscopy that uses ultrashort pulsed infrared light for better tissue penetration. The high peak energy of these laser pulses has raised concerns about nonlinear photodamage resulting from multiphoton processes. Here, we show that not only the pulse energy but also the time-averaged laser power matters in a practical biological experiment. At wavelengths and with laser powers commonly used in current neuroscience, aberrant Ca^{2+} signaling occurs as a consequence of direct infrared light absorption, that is, heating. To counteract brain heating, we explore a strategy that uses even shorter, more energetic pulses but a lower time-averaged laser power to produce the same image quality.

INTRODUCTION

Two-photon (2P) excitation fluorescence microscopy (1) is the method of choice for imaging structural and functional dynamics in the intact brain (2–4). Addressing the role of genetically identified cell populations in a circuit-specific manner has become possible through the advent and improvement of genetically encoded Ca^{2+} indicators (GECIs) (5–7). Considerable efforts are being made to enhance the speed, spatial resolution and field-of-view of 2P Ca^{2+} imaging, but for a given GECI, the user has to trade off gains in one of these parameters against losses in others, unless the number of excitation spots and/or the average laser power $\overline{P}$ per spot are increased.

2P fluorescence excitation requires high instantaneous peak intensities, which has prompted concerns about nonlinear photobleaching (8) and photodamage (9,10), resulting from excited-state absorption in the high-intensity focus. Several studies have established a steep intensity threshold for this nonlinear damage. However, from a (neuro-) physiologist's standpoint, overt morphological tissue damage as much as irreversible alterations (like those apparent on ex vivo immunofluorescence) are a late, and probably too late, criterion for assessing biological damage.

Submitted May 15, 2020, and accepted for publication October 7, 2020.
*Correspondence: martin.oheim@parisdescartes.fr
Editor: Brian Salzberg.
https://doi.org/10.1016/j.bpj.2020.10.027

Therefore, we sought for a subtler and perhaps reversible indicator of altered physiology. We used the occurrence of aberrant, light-induced Ca^{2+} signals as a sensitive readout, similar to earlier studies on neurons (9–11). In the 2P microscopy field, average laser powers of the order of tens of mW per excitation spot are generally being considered harmless (11) and up to 250 mW have been reported safe in multispot excitation schemes (12). Yet, how different pulse parameters (pulse length, interpulse interval, and peak power) affect this damage threshold has remained controversial.

In the current work, we report on a photodamage that does not involve 2P absorption, affects physiological astrocytic Ca^{2+} signals, occurs upon 920-nm excitation at low mW powers, and likely involves a local, heating-mediated damage mechanism. Unbiased automated analysis of Ca^{2+} signals revealed a subtle but measurable build-up of spontaneous, microdomain Ca^{2+} activity in the fine processes of GCaMP6f-expressing cortical astrocytes during minute-long recordings routinely used for 2P brain imaging. Near-infrared (NIR) illumination initially just increased the frequency while only slightly affecting the amplitude and cellular-volume fraction encompassed by these Ca^{2+} transients. Their frequency increase occurred without detectable morphological damage. This build-up of aberrant Ca^{2+} signals was followed by large Ca^{2+} transients in the otherwise silent soma. Pausing acquisitions for 10 min stalled light-induced Ca^{2+} hyperactivity and restored a pre-illumination baseline activity. Longer, less energetic pulses and higher average power (resulting in the same signal) were equally if not more harmful. As pulse stretching did not reduce the photo-induced Ca^{2+} signals, as would have been expected for a nonlinear damage mechanism, we postulated a lower damage power exponent ($m < 2$) and consequently investigated a linear (i.e., heating-mediated) damage process. Consistent with a single-photon absorption process, we found that even nonpulsed, continuous-wave (CW) 920-nm illumination was equally damaging to small astrocyte processes as were fs pulses.

Taken together, our experiments demonstrate that one-photon NIR absorption, in addition to nonlinear damage, can be a major limiting factor in the now commonly used wavelength band above 900 nm. This has important consequences for imaging fluorescent proteins and protein-based functional indicators as well as for studies using NIR stimulation for optogenetic activation. The careful optimization of the pulse length together with a reduction in the average laser power better preserves the biology under study.

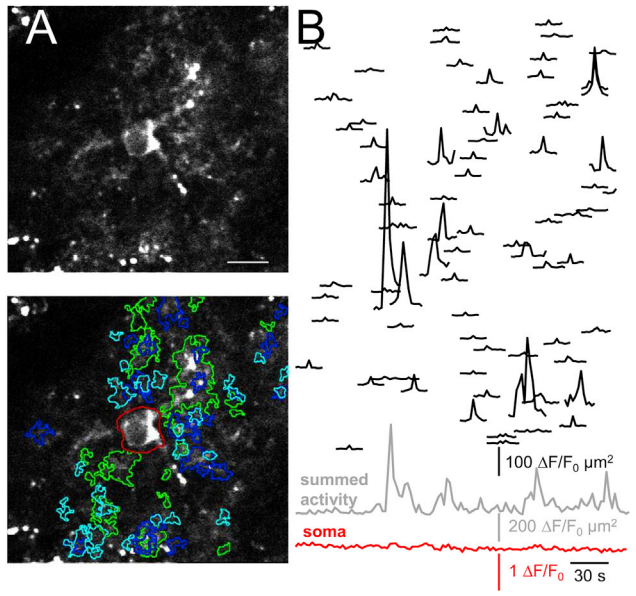

FIGURE 1 Properties of spontaneous astrocyte Ca^{2+} signals. (*A*) Diffraction-limited 920-nm excited two-photon (2P) fluorescence image across a single equatorial plane of a GCaMP6f-expressing astrocyte in an acute mouse brain slice of the barrel cortex. Imaging depth ~83 μm. Top: morphological overview from the time-average of 120 consecutive frames, taken at 0.5 Hz. Bottom: regions of interest (ROIs) corresponding to the detected Ca^{2+} transients (color for better discrimination) are shown. Overlapping ROIs indicate activity occurring in the same area at different time points. Red, central ROI shows the soma. Scale bar, 10 μm (see Video S1). (*B*) Black traces represent area size-scaled fluorescence transients of spontaneous Ca^{2+} events (i.e., $\Delta F/F_0$ multiplied by the area of the corresponding ROI) ordered, from top to bottom, according to their distance to soma. See Fig. S2 and Materials and Methods for details on the detection algorithm. Bottom (*gray*): summed activity over all events in the astrocyte processes is shown. Red trace represents somatic activity. The soma was silent throughout the recording. To see this figure in color, go online.

MATERIALS AND METHODS

Transgenic mice

All experiments followed institutional (CNRS) and European Union guidelines for the care and use of laboratory animals (Council Directive 2010/63/EU). For astrocyte Ca^{2+} imaging, we bred mice that selectively expressed the GECI GCaMP6f in astrocytes (Fig. 1; Fig. S1). For that, we crossed a floxed reporter mouse line expressing GCaMP6f in the ROSA26 locus (Ai95D; Rosa-CAG-LSL-GCaMP6f; JAX stock no. 028865; The Jackson Laboratory, Bar Harbor, ME) (13) with an astrocyte-specific cre driver line Tg(Glast-CreER^{T2})45–72 (14). For Fig. 5, inositol 3-phosphate (IP_3) receptor (IP_3R) type-2 (IP_3R2) knockout (KO) mice (15) were crossed into the GLAST-creER^{T2}::Rosa-CAG-LSL-GCaMP6f line in two steps. This generated homozygous IP_3R2-KO mice expressing GCaMP6f selectively in astrocytes. As a first step, heterozygous IP_3R2-KO::GLAST-creER^{T2} mice and heterozygous IP_3R2-KO::Rosa-CAG-LSL-GCaMP6f mice were generated. As a second step, these two lines were crossed to obtain homozygous IP_3R2-KO mice expressing GCaMP6f selectively in astrocytes. The genotype (homozygous IP_3R2-KO) was systematically verified by PCR on the day of the experiment. Cre recombinase activity was induced by a single intraperitoneal injection of 1 mg of 4-hydroxy-tamoxifen (Santa Cruz Biotechnology, Dallas, TX), diluted in corn oil, between postnatal days (P)14 to P18.

Acute brain slice recordings

P33–P46 mice were decapitated, and their heads were transferred to ice-cold artificial cerebrospinal fluid (ACSF) containing (in mM) NaCl 126, KCl 1.5, KH_2PO_4 1.25, $NaHCO_3$ 26, $CaCl_2$ 2, $MgSO_4$ 1.5, glucose 10, NaPyruvate 5, ascorbic acid 0.5, and L-glutathione 1, and bubbled with 95% O_2 and 5% CO_2. 350-μm thick coronal slices of the S1 barrel cortex were cut on a vibratome (HM 650V; Thermo Fisher Scientific, Waltham, MA) in ice-cold

slicing solution, containing (in mM) potassium gluconate 130, KCl 15, EGTA 0.2, HEPES 20, glucose 20, NaPyruvate 5, ascorbic acid 0.5, L-glutathione 1, and AP-5 (50 μM), adjusted to pH 7.4 with NaOH. Slices were transferred for 1 min to a mannitol-based recovery solution at 33°C, containing (in mM) D-mannitol 225, KCl 2.5, NaH_2PO_4 1.25, $NaHCO_3$ 26, $CaCl_2$ 0.8, $MgCl_2$ 8, glucose 20, NaPyruvate 5, ascorbic acid 0.5, and L-glutathione 1 (16). They were then incubated for 30 min in ACSF at 33°C. For recordings, the slices were placed in a ~1 mL volume chamber and perfused at 4 mL/min with prewarmed ACSF. The final temperature in the bath was 31–34°C, measured with an electronic bath thermometer. We did not separately heat the large low-magnification, high-NA objective that hence acts as a heat sink. Unless otherwise stated, the recording solution did not contain tetrodotoxin (TTX). A small sliver harp with nylon wires glued to it maintained the slice stable in the perfused chamber during recording. Mechanically instable recordings were discarded.

Immunofluorescence

The selective expression of GCaMP6f in astrocytes as well as the fraction of cells expression the GECI were quantified in slices using standard immunofluorescence and epifluorescence or confocal microscopy (see Supporting Materials and Methods).

2P microscopy

Details of our homebuilt 2P microscope are published (17), and methods specific for this study are found in the companion article (E. Schmidt, M. van 't Hoff, M. Oheim, unpublished data). Briefly, the attenuated and expanded beam of a fs-pulsed laser (MaiTai HP; Spectra-Physics Newport, Mountain View, CA) was scanned (Yanus IV; TILL Photonics, Gräfelfing, Germany) and focused with a low-magnification high-NA ×20/0.95w XLMPlanFluor dipping lens (Olympus, Hamburg, Germany) (18). The mean laser power ($\overline{P}$) was measured in air after transmission through the objective using a Coherent FieldMate powermeter with PM10 measurement head. Pulse lengths were controlled with a motorized extracavity GDD compensation module (DeepSee; Spectra-Physics Newport) and measured in the sample plane by aid of an in-line autocorrelator with external measurement head (Carpe; Angewandte Physik und Elektronik, APE, Berlin, Germany). 2P fluorescence was excited at 920 nm (with 90- or 172-fs pulse length in the sample plane, respectively), extracted with a custom 2 mm-thick large-format dichroic (700DCXXR short pass; AHF Analysentechnik, Tübingen, Germany), transmitted laser light rejected with a 680 short-pass filter (Semrock, Rochester, NY), and the remaining fluorescence funnelled through a 6-mm core diameter liquid-light guide (Lumatec, Deisenhofen, Germany) to an external, nondescanned detector box (17). This detection optics is projective, not imaging, and it maintains the étendu for optimal collection of multiple scattered fluorescence photons (18). GCaMP6f fluorescence was detected in the green channel through an ET510/80 (Semrock) emission filter and 1-mm BG22 infrared (IR) blocking filter on a side-on R6357SELECT photomultiplier (Hamamatsu Photonics, Toyooka, Japan) with homebuilt amplifiers and electronics. For each cell, we acquired a time-lapse image series of 500 frames (at 0.5 Hz) from a single equatorial plane encompassing the soma at a diffraction-limited resolution. The pixel size in the specimen plane was 146 nm. Dwell time/pixel was 6.13 μs (⇔;163 kHz scan rate). Average laser powers in the recording plane were 17.3 ± 2.7 mW (mean ± SD) for 90-ms pulses, and astrocyte soma were located, on average, at 78 ± 14 μm below the slice surface. This power requirement was a consequence of the dim basal fluorescence of GCaMP6f. For comparison, <5 mW were required for imaging EGFP-expressing astrocytes in an Aldhl1-GFP-expressing mouse line at similar imaging depths (data not shown). Image sizes were slightly different from one cell to another, as a consequence of the variable in-plane morphology of the imaged astrocyte, with a mean and SD area of (4209 ± 590) μm^2, typically some 70 μm by 70 μm.

Disruption of laser mode-locking

To compare the effects of 920-nm pulsed and CW illumination, the passive intracavity mode-locking of the MaiTai laser was hindered by narrowing the motorized tunable slit aperture inside the laser cavity via software control. The slit motor position was tuned from the initial 450 arbitrary units to 220 arbitrary units. Narrowing the slit resulted in a gradual pulse broadening that finally switched to CW operation (Fig. S5 *A*). As expected, this disruption of mode-locking (dubbed "de-mode-locking" in the figures) was accompanied by a narrowing of the spectral width (Fig. S5 *B*), measured with a fiber-coupled spectrometer (CCS 100; Thorlabs, Newton, NJ). The resulting slightly asymmetric pulse spectrum provokes a slight shift in the output wavelength that we compensated for by setting the target wavelength to 933 nm, which eventually resulted in a pulse spectrum centered at 920 nm. The de-mode-locking via partial beam obstruction reduced the laser output power so that we compensated for the power loss by augmenting the acousto-optic modulator transmittance so as to keep the average power at the objective constant under fs-pulsed and CW conditions (Fig. S6). In addition to pulse-length and spectral measurements, we directly ascertained the loss of mode-locking by confirming the loss of 2P-excited fluorescence before experiments from a green fluorescent Chroma test slide (data not shown) before we imaged cells. During the "pump-probe" protocol (Fig. 4), we interleaved a pause of 30 s between all recording episodes (de-mode-locked, optimized pulses, and shutter closed) to allow for the wavelength shift as well as the narrowing/reopening of the intracavity slit and stabilization of the laser operation and output.

Quality control and data rejection

Given the tiny structures studied, micrometric lateral or axial slice movements can result in drift and defocus, respectively, that falsify the assignment of pixels to Ca^{2+} signals and hence adversely influence the event detection during the relatively long recordings. We therefore systematically verified the quality of each recording. To this end, we generated averages in the form of two "ministacks" of 60 frames each, at the beginning and end of the 500-frame recording, respectively. Their average-intensity projections were overlaid in red/green pseudocolor and inspected for movement and defocus by comparing the position and sharpness of fine morphological features. To exclude bias, the person validating the data was unaware of the recording condition and the occurrence (or not) of Ca^{2+} signals on the respective image stack. On this basis, we excluded 2/10 cells for 90-fs pulses and 2/9 cells for the longer 172-fs pluses (data shown in Figs. 1, 2, and 3; Figs. S3 and S4). For the de-mode-locking experiments, we rejected 4/12 cells; for the laser-shuttered ones, 6/14 cells; for pulsed 90-fs imaging, 3/10 cells; and for the IP_3R2-Kos, 1/4 cells were excluded, respectively (data shown in Figs. 4 and 5; Fig. S6).

Unbiased machine-based Ca^{2+} event detection

For analyzing spontaneous Ca^{2+} signals, we programmed an automated, user-supervised, event-based detection algorithm in ImageJ (Fiji distribution (19–21), see Fig. S2). As a first step, intensity background was removed by subtracting the mean intensity measured in a user-selected cell-free area. Noise outliers were removed by "outlier removal" filtering (radius 1, threshold for removal of outlier: 1500 cts above the median). As the pixels belonging to a region of interest (ROI) defining a Ca^{2+} transient on a given frame still displayed very heterogeneous intensities, we needed to spatially filter the data without losing information to permit automated ROI selection. However, a median filter removed smaller regions or disconnected regions, whereas an average/Gaussian filter increased noise variations. After careful inspection of the raw data, it became clear that the sought information is not only contained in the intensity value of individual pixels but in the density of pixels showing higher than baseline values in a given area.

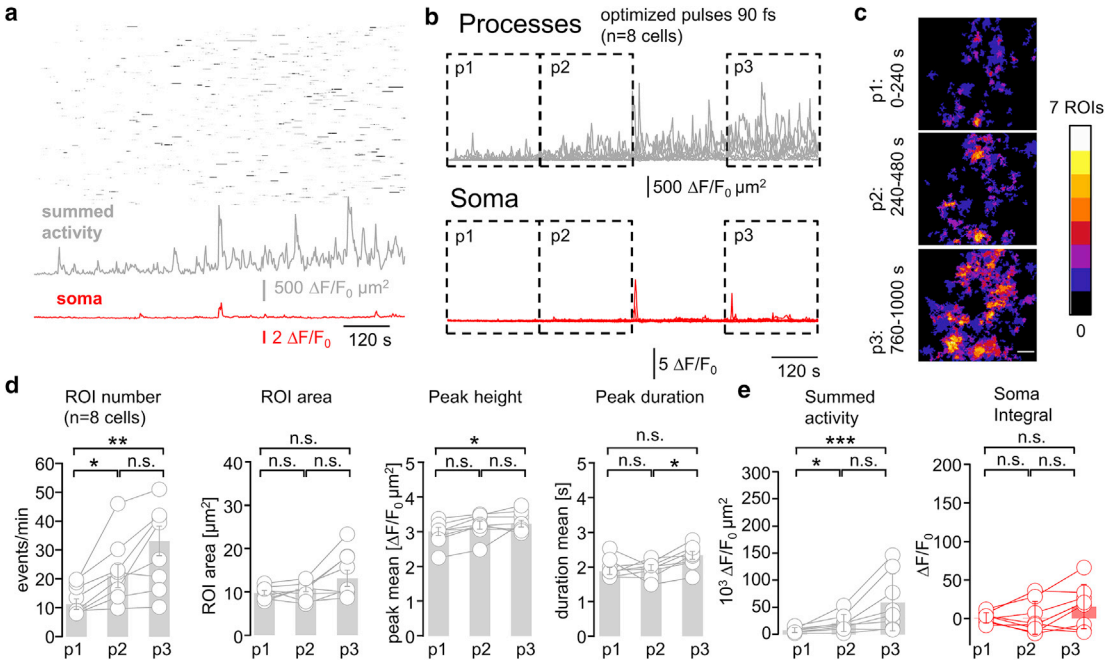

FIGURE 2 2P excitation at 920 nm triggers a subtle but discernable Ca^{2+} hyperactivity. (*A*) Black shows raster plot of the data in Fig. 1 *B*, along with its further evolution during a recording lasting more than 16 min (500 frames, 0.5 Hz). Gray represents an increase of the summed activity over all processes. Red shows that the initially silent soma becomes progressively active. (*B*) Shown are summed peripheral (*gray*) and somatic (*red*) activities under the same conditions as in (*A*) for $n = 8$ cells in $N = 6$ mice. Mean activity was quantified during periods *p1*: 0–240 s, *p2*: 240–480 s, *p3*: 760–1000 s, and boxed. (*C*) Shown is a pseudocolor overlay of the events detected during *p1*, *p2*, and *p3* for the cell in (*A*). Ca^{2+} activity increasingly occurs at similar spatial locations during *p2* and *p3*. Scale bars, 10 μm. (*D*) Shown are parameters characterizing Ca^{2+} transients during *p1*, *p2*, and *p3*. Bar plots show population mean ± SE, and symbols graph individual cells. Ca^{2+} microdomain frequency increases from *p1* to *p2* and between *p1* and *p3* (two-sided nonparametric Wilcoxon Mann-Whitney two-sample rank test). Light-induced Ca^{2+} signals resemble spontaneous Ca^{2+} microdomains, which makes them difficult to distinguish. (*E*) Gray shows a comparison of the summed activity in the astrocyte processes, i.e., integral of the traces shown in (*B*), reveals a net increase between *p1* vs. *p2* and p1 vs. *p3*. Red shows the somatic activity, corresponding to the red traces in (*B*), and remains significantly unchanged during all recording periods, although a trend to progressively higher activity is seen. $*p < 0.05$, $**p < 0.01$, $***p < 0.005$, n.s., not significant. To see this figure in color, go online.

This is plausible because for two equally large ROIs (one devoid of, the other displaying a Ca^{2+} transient), shot noise can produce in the former ROI pixels having similar intensities than those corresponding to a (small) Ca^{2+} transient, but noise pixels will rarely be nearby and will rather be scattered randomly. Therefore, for segmenting ROIs, on the background-subtracted and outlier-removed images, all pixels >0 were set to 255 to give signal-containing pixels equal weight (Fig. S2 *C*). This now binary image mask was Gaussian filtered ($\sigma = 2$ px) to smooth the contours. At this stage, we still could not use a simple intensity-based thresholding approach to identify events. The reason is that the baseline (i.e., resting) fluorescence of the soma and of the large processes is similar, if not higher, than the peak intensity of Ca^{2+} events occurring in the fine processes (see solid arrowhead in Fig. S2 *D*; compare fluorescence intensity of the soma and the Ca^{2+} event). The reason for this is obvious; because of their dimensions of the order of 100 nm or even less, the volume occupied by the fine processes fills only a fraction of the 2P excitation volume (~1 fL = 1 μm^3), which results in a lower fluorescence compared to the signal coming from the soma and large processes, for which the entire 2P excitation volume resides fully in a sea of fluorophores (Fig. 1). Instead of applying a uniform threshold, we first subtracted from each frame of the time-lapse recording the time-averaged fluorescence of the first 10 frames. This removed the bright structures that have a higher baseline fluorescence including the soma (see open arrowhead in Fig. S2 *E*), but it kept the active regions unchanged. From that, we could threshold the image stack.

Next, to selected the contours of the ROIs, we binarized each frame using as a threshold the mean intensity of all pixels having a fluorescence >0 on the first 10 frames plus three times its SD (Fig. S2 *F*). On the resulting binary image, holes in ROIs were filled to unity. Additionally, to only keep activity in the processes, the somatic region was blanked to 0. Next, frame per frame, the contours of all regions >3 μm^2 were automatically selected. As a Ca^{2+} transient typically extends over several frames and the contours change from one frame to another, a choice had to be made as to which of the time-dependent contours ROI(t) to retain. To avoid different ROIs on consecutive frames, we implemented a routine that kept only the biggest one, reasoning that this choice corresponded to the frame showing the peak of the Ca^{2+} event (an example is seen on Fig. S2 *G*, for the event identified on frame #87, similar ROIs related to the same transient are also detected on frames #83, #84, #85, #86, #88, and #89, respectively. The ROIs all spatially and temporally overlap with the ROI on frame #87.) Traces showing the evolution with the time of the Ca^{2+}-dependent 2P fluorescence, $\Delta F/F_0(t)$, were generated by taking the mean fluorescence of the finally chosen ROI. Here, F_0 corresponds to the baseline fluorescence of the same region during the first 10 frames of the time-lapse recording that showed no activity (i.e., no "hot pixels" on the binary region map). The peak of the fluorescence transient defined the event time; the frames preceding or after the peak, for which five consecutive data points were dimmer than half the peak intensity, were chosen as the beginning and end, respectively, of that event. We adopted the five consecutive frame criterion to count rapid, double-peaked events as one.

After this fully automated choice of ROIs and readout of Ca^{2+}-dependent fluorescence transients, a user-controlled validation step was interleaved. For each event, the detected ROI contour was automatically superposed on the corresponding raw data image frame (to visually confirm the Ca^{2+} elevation) and on the temporally averaged stack (giving an idea of the cell morphology and to confirm its intracellular localization), and the corresponding $\Delta F/F_0$ trace was displayed for visual inspection. Artifacts

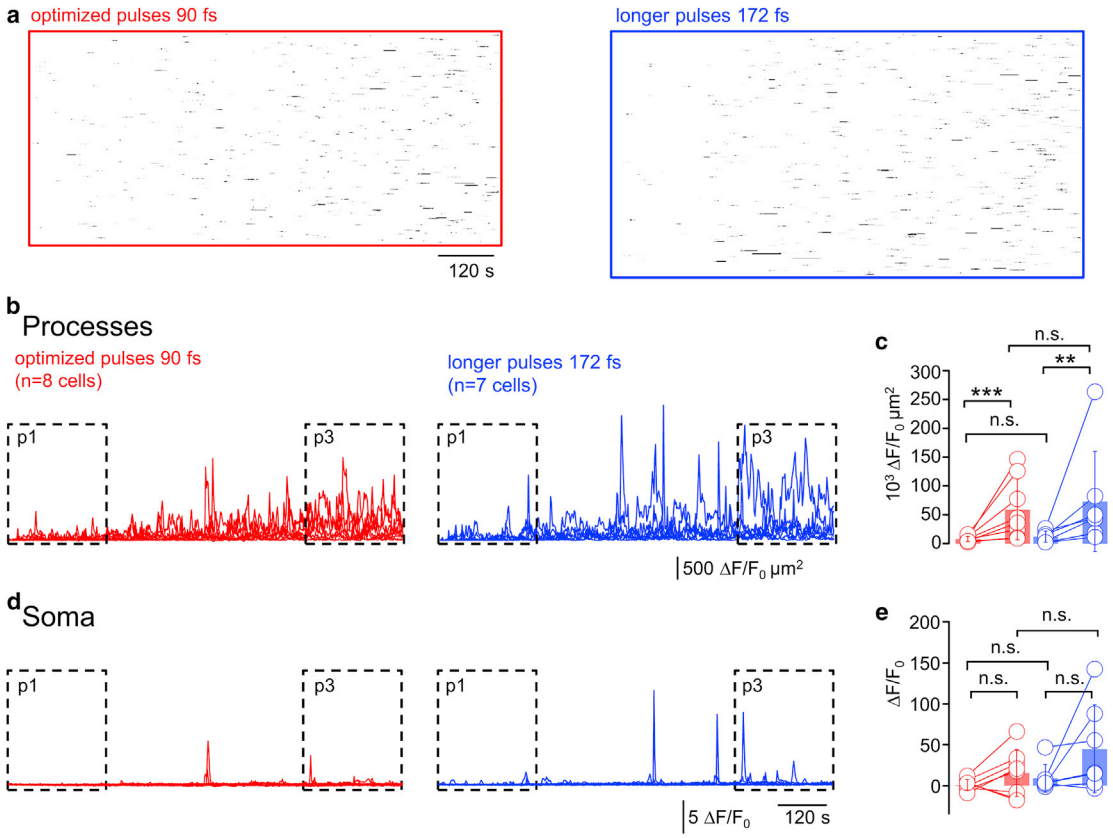

FIGURE 3 Longer, less energetic pulses do not reduce light-evoked Ca^{2+} hyperactivity. (*A*) Right: raster plot of 920-nm light-induced Ca^{2+} hyperactivity as in Fig. 2 *A* but for a different cell is shown. Pulses were carefully optimized as in the two previous figures to achieve the shortest possible pulses under the objective (see Materials and Methods), resulting in a 90-fs pulse length ($sech^2$). See Video S2 for a recording of this cell. Left: shown is the same for a cell excited with 172-fs pulses, i.e., with lower peak power but higher average laser power to maintain a constant initial signal, i.e., $\overline{P}^2/\tau = const.$ (*B*) Red shows the summed activity as in Fig. 2 *B* ($n = 8$ cells/six mice at 90 fs) and side-to-side comparison with summed activity upon 172-fs excitation (*blue*). (*C*) Ca^{2+} activities in *p3* compared to *p1* (defined as in Fig. 2 *B*) increase (mean ± SE) for both 90-fs (*red*, same data as in Fig. 2 *E*) and 172-fs pulses (*blue*, $n = 7$ cells/six mice) are shown. Activity was undistinguishable between short and long pulses for *p1* (validating our experimental paradigm) but also during *p3*, i.e., contrary to what was expected for a highly nonlinear photodamage, no significant difference was found for different pulse energies (one-sided nonparametric Wilcoxon Mann-Whitney two-sample rank test). (*D*) Shown are somatic $\Delta F/F_0$ traces for 90-fs (*red*, corresponding to Fig. 2 *B*) and 172-fs pulses (*blue*). (*E*) Statistical analysis showed that the somatic activity was indistinguishable between 90-fs (*red*, corresponding to Fig. 2 *E*) and 172-fs pulses (*blue*), both during p1 and p3. $*p < 0.05$, $**p < 0.01$, $***p < 0.005$, n.s., not significant. To see this figure in color, go online.

from bright and almost stationary bright spots (marked asterisk in Fig. S2 *B*) that could result from lipofuscin-rich granules (22) or mitochondrial autofluorescence, as well as slight movement artifacts, were easily discernible from "true" Ca^{2+} transients on the basis of their different morphology and the different temporal profile of the $\Delta F/F_0$ trace. Using this procedure, we excluded 1.3% of all detected ROIs, and we observed no significant differences among the different experimental conditions, validating the robustness of our procedure (nonparametric Kruskal-Wallis test). Finally, for the confirmed ROIs, $\Delta F/F_0(t)$ traces and the extracted parameters were automatically tabulated, and the ROIs were overlaid on the original time-lapse image stack (background and outliers removed).

The traces, the ROI area and distance from soma (defined by their centroid distance), and the baseline fluorescence, start, peak, and end time points of each Ca^{2+} event were passed on to IGOR Pro (Version 6.3; Wavemetrics, Lake Oswego, OR) for further analysis. For data compression, only a small section of the trace around the Ca^{2+} event was kept (see Fig. S2, *H* and *I*). Finally, all $\Delta F/F_0$ traces were weighed with their respective ROI area, following the rationale that a larger active area corresponds to a larger Ca^{2+} release or influx and hence should manifest as a larger level of activity compared with a smaller otherwise identical active region (Fig. S2 *J*).

For statistical analysis between different experimental conditions, we analyzed each cell separately, i.e., we did not pool Ca^{2+} events from different cells in a given condition. We deliberately made this choice to be able to detect heterogeneity in the cells' baseline activity and responses to illumination and to avoid that a single cell having a high baseline activity or showing a big increase in Ca^{2+} events in illumination could bias the comparison.

The somatic ROI was selected in ImageJ, and the corresponding intensity trace was systematically analyzed and stored, independent of whether Ca^{2+} activity was observed or not. Somatic $\Delta F/F_0(t)$ traces were generated in IGOR Pro in a two-step process. In the first step, the algorithm searched for the consecutive five-frame segment that has the lowest SD on the initial 60 frames of the recording (the rationale being that this segment contained no Ca^{2+} events). We used this segment to calculate $F_0^{(I)}$ and normalize the fluorescence trace as $dF/F_0^{(I)}$. Using this $F_0^{(I)}$, candidate somatic Ca^{2+} transients occurring on the same initial trace segment were detected (using the $F_0^{(I)} + 3$ SD criterion). Then, in a second step, a refined baseline estimate was generated from only those data points on which no peaks had been detected. This new value, $F_0^{(II)}$, was used to calculate the somatic $\Delta F/F_0^{(II)}$ trace.

For the comparison shown in Fig. S3 *B*, a single ROI compassing the entire neuropil was selected by inversion of the previously identified

somatic ROI. The mean intensity in the processes was extracted from a median-filtered (0.5-px radius) image stack (after removal of background and outliers as described before). The traces were then normalized and plotted as $\Delta F/F_0$, using the same two-step procedure as described above for the soma. The semiautomated program for Ca^{2+} event detection in ImageJ as well as the IGOR Pro scripts are available upon request.

Statistical analysis

Statistical tests were run in IGOR Pro. Data sets were compared using a nonparametric Wilcoxon Mann-Whitney two-sample rank test. For data sets with more than two conditions, a group test (nonparametric Kruskal-Wallis test, χ^2 approximation for the p-value) was performed first. Significance levels are marked in the graphs using $*p < 0.05$, $**p < 0.01$, $***p < 0.005$, and *n.s.*, not significant.

RESULTS

Spontaneous astrocyte Ca^{2+} activity increases during two-photon recordings

2P imaging upon 920-nm excitation revealed a plethora of asynchronous and spatially confined Ca^{2+} signals (Fig. 1; Video S1) in the barrel cortex of adult mice (P33–P46) sparsely expressing GCaMP6f (23) in a subset of astrocytes (Fig. 1 *A*; Fig. S1). As observed by other laboratories, these microdomain Ca^{2+} signals did neither require neuronal nor direct astrocytic stimulation, and they persisted when blocking neuronal action potentials with TTX (1 μM) (see Discussion).

We acquired a time-lapse image series from a single equatorial plane encompassing the soma. We used a sawtooth raster scan with 163 kHz pixel rate and 0.5 Hz frame rate. Given the tiny dimensions of astrocyte processes, we Nyquist sampled ($\Delta_{xy} < PSF_{xy}/2$) at a pixel size of $\Delta_{xy} = 146$ nm/px to maintain diffraction-limited spatial resolution ($B < f_s/2$, where B is the bandwidth, fs the spatial frequency, and $PSFxy$ is the lateral extent (FWHM) of the point spread function). Regions of elevated Ca^{2+} (Fig. 1 *A*, *bottom*) and their corresponding Ca^{2+} transient waveforms (Fig. 1 *B*, *top*) were extracted by an unbiased machine-based detection procedure (see Fig. S2). The "summed activity" trace indicative of the cumulative activity in the processes was dominated by a large number of small Ca^{2+} transients and a few large events, and it was otherwise flat as expected for a predominantly localized, asynchronous Ca^{2+} activity. The soma showed little, if any, spontaneous activity during the first 4 min of recording. On average, Ca^{2+} transients were rare (11.25 $\pm$ 1.76 events/min), short lived (1.90 $\pm$ 0.10 s duration), and of small amplitude ($\Delta F/F_0 = 3.02 \pm 0.12$), and they were confined to tiny subregions of individual astrocyte branches (mean area, 9.26 $\pm$ 0.52 μm^2 vs. 3969 $\pm$ 302 μm^2 total astrocyte area, i.e., individual events occupied ~0.2% of the surface area; mean $\pm$ SEM for eight cells during 4-min recording). These microdomain Ca^{2+} signals are very similar to those reported by others (24–27).

Raster plots on which we ordered active regions according to their distance-to-soma revealed Ca^{2+} transients throughout the neuropil with no obvious localization preference. However, when we extended the recording duration beyond the initial 4 min, we recognized a first subtle and then increasingly pronounced Ca^{2+} hyperactivity in the fine processes (Fig. 2 *A*, *top*). This hyperactivity was also seen as a rise of the "summed activity" trace that measures the cumulative activity within the processes (Fig. 2 *A*, *bottom*, *gray trace*). Somatic Ca^{2+} hyperactivity was observed secondary to the photo-induced signal triggered in the cell's periphery (Fig. 2 *B*, *bottom*, *red trace*). Also, with increasing recording time, astrocytic microdomain Ca^{2+} signals occurred repeatedly within the same subcellular domains (Fig. 2 *C*). Nevertheless, events remained initially relatively stereotyped in terms of their area, peak amplitude, and duration, but their frequency almost doubled ($\times$1.87) when comparing early recording periods (*p1*, 0–4 min) with later ones (*p2*, 4–8 min). After 16 min of continuous recording, microdomain Ca^{2+} transients in the processes tripled in frequency and displayed a 40% increase in dF/F_0 amplitude compared with the beginning (*p1*) (Fig. 2 *D*). Other parameters remained stable, indicating that photodamage merely triggered more events. We conclude that both event frequency ($\times$2.94) and summed activity ($\times$7.5) of the peripheral astrocyte Ca^{2+} activity are bona fide markers for light-induced Ca^{2+} hyperactivity. At the macroscopic level, longer recordings produced a net increase in somatic Ca^{2+} activity ($\times$14.5, *p3* vs. *p1*, Fig. 3 *E* and Video S2). Aberrant Ca^{2+} signals occurred in the absence of visible morphological damage, and mice expressing EGFP rather than GCaMP6f in an astrocyte-specific manner showed no detectable change (E. Schmidt, M. van 't Hoff, M. Oheim, unpublished data). Similar Ca^{2+} hyperactivity was observed in astrocytes expressing GCaMP3 (28), an earlier GECI displaying a higher basal fluorescence but reduced $\Delta F/F_0$ amplitude (29), excluding a GCaMP6f-specific effect (data not shown).

The Ca^{2+} signal obtained when lumping together the entire neuropil to one single ROI mirrored the evolution with time of the summed activity of all individual detected events in the cell periphery (Fig. S3). Thus, at least as far as aberrant Ca^{2+} signaling is concerned, the fine processes behave as a single "compartment," although they are highly branched and compartmentalized into a tortuous and diffusionally segregated volume. The soma behaves differently. Whatever the mechanism, damage initiation seems to be local.

Taken together, these first results demonstrate the vulnerability of small astrocyte processes to the exposure with pulsed NIR light at powers common to typical biological 2P microscopy. Laser powers of tens of mW routinely used in the literature trigger astroglial Ca^{2+} hyperactivity detectable in both processes and soma. Intriguingly, the illumination-induced Ca^{2+} transients initially differ little from their "physiological" counterparts but do differ in their frequency. As a first approximation, a simple "center versus surround" analysis provides a straightforward readout of

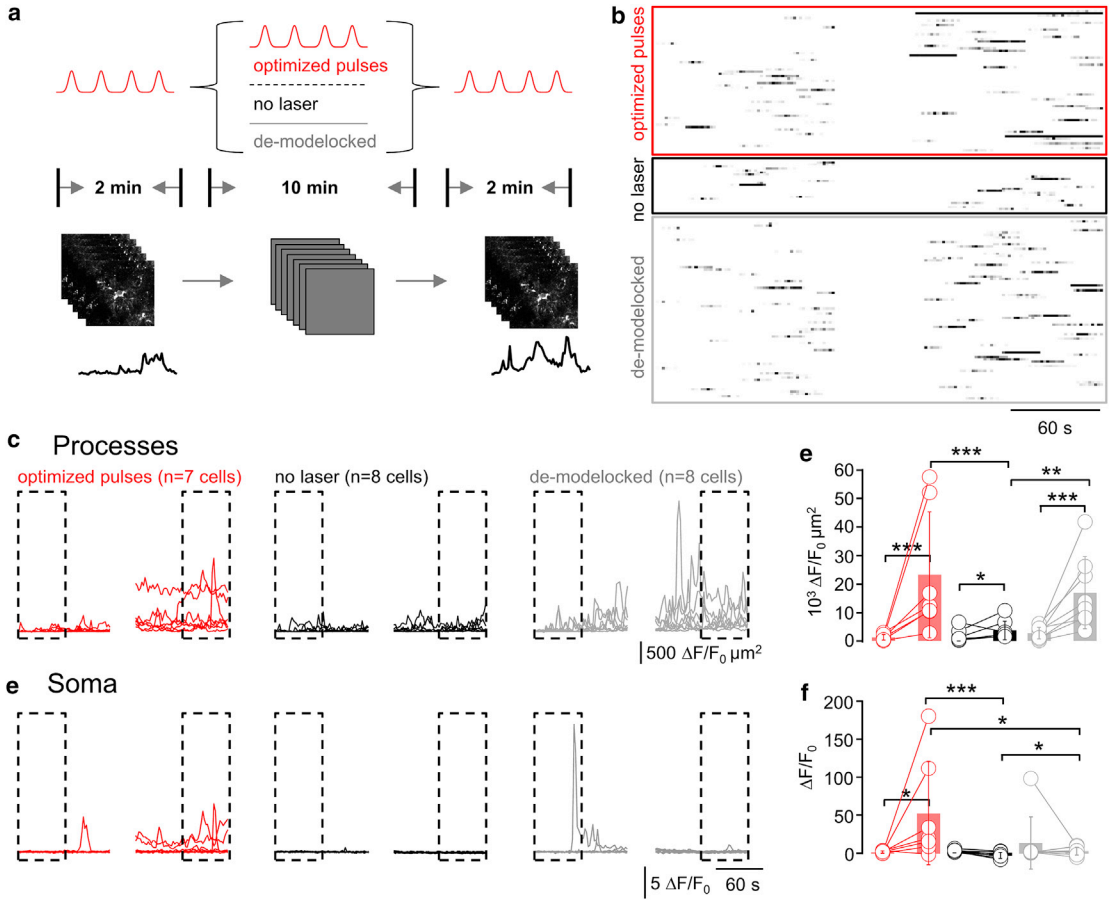

FIGURE 4 Light-induced Ca^{2+} hyperactivity depends on total light dose, not the pulse energy. (*A*) Schematic representation of the experiment design is shown. Spontaneous Ca^{2+} transients were recorded during a 2-min control period to establish a baseline activity (*p1*; 920 nm, 90 fs, 0.5 Hz). Then, during 10 min, three different protocols were applied: 1) the cells were either imaged as in the preceding figures (with the same hyperactivity scenario as before), or 2) the laser was shuttered and the cells allowed to recover from the previous recording. In a third variant, 3) we disrupted the laser mode-locking to expose the cells to continuous-wave (CW) radiation with the same average power $\overline{P}$ as during pulsed excitation (see Materials and Methods and Fig. S6). The respective impact of these different protocols on the astrocytic Ca^{2+} activity was read out in another 2-min recording (with the same parameters as *p1*). (*B*) Raster plots illustrate the outcome of the three different protocols. (*C*) Cumulative Ca^{2+} activity traces in the astrocyte processes during p1 and p3 are shown. (*D*) Statistical analysis of data was shown in (*C*). Shown are the activity increases for all conditions between the beginning of *p1* (0–60 s) and end of *p3* (660–720 s; one-sided nonparametric Wilcoxon Mann-Whitney two-sample rank test). Of note, the Ca^{2+} activity in the processes during *p3* is indistinguishable between exposures to pulsed versus CW light, both of which are significantly higher than with the laser shuttered. All experiments started from initial activity levels during p1. *n.s*, not shown for clarity. (*E*) Shown are somatic $\Delta F/F_0$ traces for the three scenarios and statistical analysis in (*F*). For CW illumination, somatic activity is significantly higher in *p3* compared to either no or pulsed excitation during *p2*, respectively. $^*p < 0.05$, $^{**}p < 0.01$, $^{***}p < 0.005$, n.s., not significant. To see this figure in color, go online.

aberrant light-induced Ca^{2+} activity in the soma and processes, respectively.

Pulse stretching does not reduce photodamage

For a given fluorophore, microscope, and signal, nonlinear photodamage can potentially be reduced by modifying either the pulse frequency f or duration τ and adjusting the average laser power $\overline{P}$ accordingly. Keeping, respectively, $\overline{P}f = const.$ or $\overline{P}/\tau^2 = const.$ will maintain a constant signal. Longer pulses will hence reduce the pulse energy but require higher $\overline{P}$.

However, whether shorter or longer pulses are per se better for biological 2P imaging has been a matter of debate. The outcome depends on whether photobleaching and photodamage increase more or less rapidly with $\overline{P}$ than the signal. Longer pulses will be neutral if damage scales with a power exponent m (i.e., $\overline{P}^m$) of two, like 2P-excited fluorescence (9), whereas pulse stretching will be beneficial if higher-order photodamage ($m > 2$) dominates (10). Conversely, longer pulses will exacerbate damage processes having a $m < 2$, e.g., when one-photon absorbers are present (30) or if tissue heating occurs (31).

We next directly compared Ca^{2+} transients upon 920-nm excitation with 90-fs (as before) vs. 172-fs pulses. We had obtained 90-fs pulses by a careful optimization of the excitation optical path and an optimal prechirping in a wavelength- and objective-dependent manner so as to attain the shortest possible pulses in the sample plane. 172-fs pulses

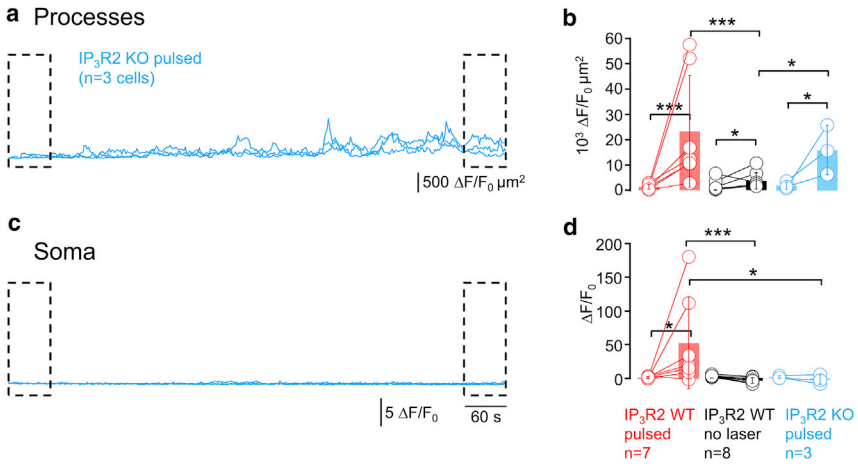

FIGURE 5 Somatic but not peripheral Ca^{2+} hyperactivity is IP_3R2 receptor dependent. (*A*) Cumulative Ca^{2+} activity in the astrocyte processes during a 12-min recording (920 nm, 90 fs, 0.5 Hz) of GCaMP6f-expressing astrocytes from IP_3R2 KO mice shows a pronounced light-induced Ca^{2+} hyperactivity in the processes ($n = 3$ cells from two mice). (*B*) Shown is the comparison of cumulative activity in the processes of IP_3R2 KO mice during the beginning, *p1* (0–60 s) and the end of the recording, *p3* (660–720 s) (*p1* and *p3* are the same as in in Fig. 4, *light blue* graphs, one-sided nonparametric Wilcoxon Mann-Whitney two-sample rank test). No significant difference is observed between either p1 or p3 between IP_3R2 KO or WT mice (data from Fig. 4 *D*), whereas the KO data during *p3* is significantly different from the same period when the laser was shuttered (data from Fig. 4 *D*), confirming that peripheral Ca^{2+} hyperactivity persisted in the absence of the IP_3-mediated signaling pathways. In contrast, (*C*) soma of IP_3R2 KO astrocytes are silent during the whole recording period in all cells. (*D*) In fact, somatic activity in IP_3R2 KO mice is more similar to the WT astrocytes that were only imaged during *p1* and *p3* with the laser shuttered in between than to those that were exposed to continuous 2P excitation fluorescence imaging (cf., Fig. 4 *F*). $*p < 0.05$, $**p < 0.01$, $***p < 0.005$, n.s., not significant. To see this figure in color, go online.

correspond to the standard "midline" manufacturer tuning of the DeepSee pulse compressor at 920 nm (see Supporting Materials and Methods; E. Schmidt, M. van 't Hoff, M. Oheim, unpublished data).

Unlike what would be expected for a nonlinear photodamage mechanism, longer pulses and higher laser power did not reduce aberrant Ca^{2+} signals (Fig. 3 *A*). In the experiments with 172-fs pulse length, we increased $\overline{P}$ by a factor of 1.26 ± 0.06 compared with 90-fs pulses so that astrocytes had an equal initial GCaMP6f signal for either pulse length (see Supporting Materials and Methods and Fig. S4 for data of the individual cells). To exclude bias, we also alternated the sequence of short and long pulses so that half of the cells were imaged first to 90- and then to 172-fs pulses and vice versa for the other half. Upon excitation with 172-fs pulses, light-induced local Ca^{2+} signals were readily detectable in the astrocyte processes (Fig. 3 *B*), and somatic activation prevailed (Fig. 3 *D*). Quantifying the activity during the initial (*p1*) and terminal 4-min segments (*p3*) revealed by and large similar results for 172- and 90-fs pulses in the processes (cumulative activity increased $\times 6.0$ vs. $\times 7.5$, *p1* vs. *p3*, Fig. 3 *C*). The overall somatic activity in *p3* was not significantly different between both pulse lengths (Fig. 3 *E*), but somatic Ca^{2+} transients arrived earlier and were of larger amplitude at 172-fs than with the shorter pulses. Our results exclude a nonlinear photodamage as a mechanism for triggering aberrant astrocyte Ca^{2+} activity.

Equal-power CW illumination at 920-nm is as damaging as fs pulses

How can we explain that stretched pulses and higher peak powers are not more damaging? We hypothesized that, contrary to common belief, in the 100-fs and 920-nm excitation regime used for most fluorescent proteins like GCaMP, NIR photodamage is not dominated by highly nonlinear processes like excited-state absorption, absorption from the triplet state, or indirect effects that occur via reactive oxygen species production through mitochondrial two- and three-photon absorption or lipid oxidation but rather through direct NIR absorption. This is plausible because both water and lipid absorption increase by more than one order of magnitude between 800 and 900 nm (Fig. S5), and so does the risk of focal heating (31,32). Thus, unlike at the shorter wavelengths (700–800 nm) (33) that have traditionally been used for 2P excitation of dyes and small chemical indicators, the longer wavelengths that optimally excite fluorescent proteins and optogenetic activators and that are now commonly used in biological 2P microscopy might result in a significantly higher absorption and a local heat production.

A simple, testable prediction for a one-photon-mediated damage process is that depositing the same average power $\overline{P}$ with a CW 920-nm laser (i.e., no pulsing) should be equally damaging as pulsed illumination with 2P fluorescence excitation. This is what we tested next after having ascertained the effectiveness of a software-based disruption of mode-locking of our Ti:Sapphire laser (see Materials and Methods and Fig. S6, *A* and *B*).

To permit a direct comparison, we designed a "pump-probe" experiment, in which we first imaged GCaMP6f-expressing astrocytes during 2 min with 90-fs pulses to establish a baseline activity for each cell. We then pursued during 10 more minutes with either pulsed or CW illumination (at the same $\overline{P}$). As no fluorescence is excited when pulsing is disrupted, we read out the resulting Ca^{2+} activity

during another 2-min "probe" period with pulsed excitation at the end of each recording. In a third variant (negative control), we simply shuttered the laser during the 10-min interval to allow the cells to recover before reading out the activity again in the terminal 2-min period (Fig. 4 *A*). For each cell, we graphed raster (Fig. 4 *B*) and cumulative activity plots (Fig. 4, *C* and *E*) similar to the earlier figures.

As before (cf., Figs. 2 and 3), ongoing fs-pulsed illumination triggered synchronized peripheral Ca^{2+} activity (Fig. 4 *D*) as well as somatic Ca^{2+} signals (Fig. 4 *F*). As predicted for a linear damage mechanism, CW illumination produced an amount of peripheral Ca^{2+} hyperactivity that was indistinguishable from pulsed excitation (Fig. 4, *D* and *F*, *gray traces*). Shuttering the laser between acquisitions virtually abolished this light-induced activity, indicating that the total light dose, not a once triggered and then irreversible progressing damage cascade, produced the aberrant Ca^{2+} signals (Fig. 4, *D* and *F*, *black traces*). Interestingly, and very different from the behavior of the astrocyte processes, CW illumination did not produce measurable somatic hyperactivity, suggesting that some structure or organelle predominantly located in the cell body can be sensitized by fs-pulsed but not continuous NIR illumination (Fig. 4 *F*). Together, our data provide compelling evidence for laser-induced one-photon damage being a source of peripheral astrocyte Ca^{2+} hyperactivity.

Somatic but not peripheral photodamage is IP_3R mediated

What is the reason for the different damage mechanisms in the processes and soma? Perhaps reactive oxygen species affect Ca^{2+} handling by oxidation of the IP_3R and sensitization of endoplasmic reticulum Ca^{2+} release to promote perisomatic Ca^{2+} oscillations, mitochondrial Ca^{2+} uptake (34), and release (35). As the IP_3R type-2 (IP_3R2) is thought to be the major, if not only, IP_3R expressed in astrocytes (36), we took advantage of an available IP_3R2 KO mouse strain (15) to breed mice expressing GGCaMP6f in astrocytes devoid of IP_3R2. Homozygous mice allowed us to test if IP_3R sensitization was involved in mediating the somatic damage. As spontaneous Ca^{2+} signals persist in the processes in IP_3R2-KO mice (37), we speculated that imaging-evoked somatic and peripheral Ca^{2+} signals could be distinguished through their IP_3R2 dependence. As before, we ascertained for all experiments equal $\overline{P}$ (Fig. S6 *C*) and equal mean GCaMP6f fluorescence at the beginning of the recordings (Fig. S6 *D*).

Time-lapse 2P imaging of spontaneous Ca^{2+} activity in GCaMP6f-expressing astrocytes in slices of IP_3R2-KO mice produced heat-induced microdomain Ca^{2+} transients in the cell periphery much as in the wild-type (WT) (Fig. 5 *A*). In stark contrast, the somatic Ca^{2+} hyperactivity was abolished (Fig. 5 *C*). Statistical analysis of the initial and terminal 1-min segments confirmed light-induced Ca^{2+} activity in the processes of astrocytes from IP_3R2-KO mice (*blue* on Fig. 5 *B*). This increase was significant, both compared with the beginning of the same recording and with respect to the second period in WT mice when shuttering the laser (data reproduced from Fig. 4 *D*). However, different from WT mice, the same robust peripheral Ca^{2+} hyperactivity failed to trigger somatic responses in KO mice, confirming the involvement of perisomatic but not peripheral IP_3R in the build-up of somatic light-induced Ca^{2+} transients.

DISCUSSION

We used state-of-the art methods to image and analyze microdomain Ca^{2+} signals in cortical astrocytes to show that 1) 2P imaging under conditions usually considered noninvasive led to an increase in spontaneous astrocyte Ca^{2+} activity; 2) at constant signal ($\overline{P}^2/\tau$ = const.), stretched pulses and a correspondingly increased average power failed to reduce this light-induced hyperactivity, excluding damage mechanisms with a power exponent $m > 2$; 3) 920-nm nonpulsed (CW) excitation at the same $\overline{P}$ evoked aberrant microdomain Ca^{2+} signals in astrocyte processes with comparable efficiency than pulsed excitation, confirming a one-photon absorption mechanism; and 4) genetic ablation of the major astroglial IP_3R abolished somatic Ca^{2+} transients, but it did not affect the heat-mediated hyperactivity in the fine processes, pointing to different damage mechanisms in the cell body and periphery.

Irreversible photodestruction or reversible modification of Ca^{2+} homeostasis

Our data show an increase in the spontaneous activity in astrocytes subsequent to minute-long exposures of pulsed and CW 920-nm light (Figs. 2, 3, and 4). When limiting the initial exposure (60 frames over 2 min acquired at diffraction-limited resolution and 159 kHz scan rate), this light-induced hyperactivity was reversible over a 10–12-min recovery window (Fig. 4, *C* and *E*, *middle*). Longer recordings led to permanently increased GCaMP fluorescence in the scanned region, to increased spiking, and eventually, to an uncontrolled build-up of Ca^{2+} transients and increase in resting Ca^{2+}. This pathological hyperactivity is clearly prohibitive for studying the subtleties of Ca^{2+} microdomain signaling, and we consider a subtle deviation from unperturbed baseline activity as sufficiently invasive for discarding such recordings. The transient alterations observed in astrocyte Ca^{2+} homeostasis are reminiscent of the illumination-induced changes in neuronal firing rates, and they constitute a finer readout of light-induced adverse effects than those picked up by immunofluorescently monitored activation of astrocytic or microglial markers, heat shock protein, or activated caspase-3 16 h after a 20-min illumination episode at high laser power (>250 mW) (31).

Brain heating as a damage mechanism

Heating was considered as a possible damage mechanism even before the advent of the 2P microscope (38). Sheppard predicted permissive $\overline{P}$ delivered to a single excitation spot around 35 and 100 mW for stationary illumination and fast scanning, respectively. These values seem optimistic relative to reported experimental damage thresholds that are closer to 10 mW in single-spot nonresonant scanning geometries (9–11). Comparing fs versus ps pulses, Schönle and Hell judged focal heating irrelevant at 750–800 nm (the then dominant spectral window for exciting small-molecule chemical indicators), but neither did they use a biological readout, nor is it clear if small cellular compartments or subcellular organelles would resist to the predicted 0.5–3°C-change calculated by their model (33). On the other extreme, König and co-workers reported that visually detectable morphological damage of unlabeled cultured cells exposed to fs and ps pulses (at 780 nm, 60-μs pixel dwell time, NA 1.3) followed an approximate $\overline{P}^2/\tau$ law, suggesting a power exponent close to $m = 2$ (30). Subtler forms of photodamage than visible destruction were not assessed in that study. At longer wavelengths, Macias-Romero et al. estimated a 1–5°C increase in the focus of a 1035-nm laser beam (80 MHz, 1.1 NA) in water for pixel dwell times <10 μs (39), and the authors argued in favor of wide-field illumination and low-repetition rate 2P imaging to mitigate thermal damage. Using the temperature-dependent Stokes shift of Laurdan, a 1°C/100 mW change was measured for a CW 1064-nm trapping beam in the 20- to 200-mW regime (40). Along the same lines, Schmidt and co-workers predicted a temperature rise around 5°C/100 mW for various IR trapping beams based on a model taking into account light absorption in the neighborhood of the focus, outward heat flow and heat sinking by the glass surfaces of the sample chamber (41). A ΔT of a similar order of magnitude (1.8°C/100 mW) was measured with thermocouple probes and quantum-dot nanothermometers upon 2P single-spot scanning in the neocortex of awake or anesthetized mice, in vivo, and $\overline{P} > 250$ mW produced irreversible thermal destructions (31). Recently, the Emiliani lab modeled and measured 2P-induced heating to predict bounds for safe conditions of spiral scan and digital holography photoactivation. They predicted a 2°C temperature rise produced by a 3-ms illumination with 100 holographic spots at the photostimulation conditions necessary to evoke an action potential in vivo (42).

In this broader context, our results underpin the relevance of thermal damage for two-photon imaging in the biologically important spectral window around 920 nm and call for a necessary degree of caution when designing and interpreting experiments using 2P microscopy and photostimulation. Wavelengths above 900 nm and in the μm regime are commonly being used for the two- and three-photon excitation of fluorescent proteins, GECIs, and for the optogenetic activation of opsin-expressing cells. NIR light at these wavelengths is potentially more invasive than previously thought, particularly when imaging at high spatiotemporal duty cycles or when using multiple-spot schemes that increase the total power deposit in tissue.

As thermal effects rely on the accumulation and dissipation of energy, they depend on λ and $\overline{P}$ but also on other parameters like the imaging depth, the precise tissue geometry (culture, slice, in vivo), the scanning parameters, and the pulse frequency and shape. Moreover, the heat deposit will be additive or even supralinear in multispot, line illumination, and holographic illumination schemes (43) and when sampling with high spatial and temporal frequencies because nearby spots and high duty cycles will further intensify the heat that cannot dissipate into neighboring colder tissue volumes. On the other hand, external factors like brain cooling due to a cranial window (44), a room-temperature water dipping objective, or perfusion with temperature-controlled ACSF might contribute to equilibrating temperature gradients, at least for near-surface imaging.

At a fixed pulse length, we expect lower pulse repetition rates, shorter pixel dwell times, and rescanning (i.e., temporal averaging on a μs timescale) (45) to be beneficial. In view of thermal diffusion rates of $\sim$1 $\mu m^2/\mu s$, random-access scanning schemes in which neighboring pixels are excited in a spatially interspersed manner rather than sequentially scanned will favor the dissipation of locally generated heat. An overall low overall duty cycle (i.e., the recording from multiple, distant, and small ROIs rather than from full frames or the use of short bursts of acquisitions taken at high frequency rather than continuous streaming of images (31)) should be beneficial to mitigate build-up of thermal damage. Random-access scanning (46–48) will be particularly useful in applications in which dense spatiotemporal sampling is indispensable like when imaging dendritic spines, astrocyte processes, or in applications of 2P stimulated emission depletion microscopy that inevitably goes along with even higher spatial frequency sampling.

Linear versus higher-order damage

Our work alerts the biological microscopist to the importance of other damage mechanisms that coexist with localized nonlinear photodamage (10,49) that is fairly well described in the literature. Of note, one has to distinguish between linear damage mechanisms in which (whatever observable is used for quantifying damage) the measured damage depends linearly on $\overline{P}$ and one-photon mediated damage, which must not necessarily be linear. For example, photodamage by blue visible light or ultraviolet is typically nonlinear, e.g., when reducing equivalents are overwhelmed by radical production. We here show that NIR light-induced Ca^{2+} hyperactivity depends on the average rather than peak power, thereby identifying a one-photon-mediated process. However, just because damage does not require two-photon

excitation, it does not follow that it is linear, and we did not establish a linear power law.

The simplest conclusion from our results is that photoinduced astrocytes microdomains are produced by a heating-mediated mechanism. Our work therefore calls for some prudence in the ongoing quest for ever-longer wavelength IR-excited and red-shifted probes for deep tissue imaging because both water and lipid absorption (μ_a) continue to increase at longer wavelengths. On the other hand, as tissue scattering (μ_s) is reduced at these wavelengths, the choice of the optimal fluorophore and excitation wavelength windows will be a compromise between absorption and scattering (50,51).

Thermal damage is a particular concern for deep tissue imaging because compensating for the exponential excitation losses with increasing depth will expose the tissue surface to very high laser powers that, even unfocused, will be harmful because of surface heat generation. On the other hand, at moderate imaging depths in vivo, the perplexing situation can arise that surface cooling dominates so that the largest temperature increase will be measured beneath the focal plane (31). Therefore, once again, the precise outcome will depend on the average power, wavelength, and experimental geometry.

Somatic Ca^{2+} signals are a sensitive readout for damage

Although somatic Ca^{2+} transients have been used as a proxy for astrocyte activity, $\geq$90% of spontaneous Ca^{2+} activity occurs in the cell periphery (24,27,43,52,53). We find (Figs. 1 and 2) that in cortical slices, astrocyte somata were mostly silent under conditions of 2P imaging that preserve physiological Ca^{2+} signaling. Somatic Ca^{2+} signals were sparse, and this blocks, both in experiments with 1 μM TTX in the bath and without neuronal action potential, making their occurrence a sensitive and facile readout for imaging-related damage.

Fine astrocytic processes have temperature-dependent calcium dynamics

In our experiments, aberrant somatic Ca^{2+} were systematically secondary to peripheral activation. Although we cannot exclude that only the small compartments are sensitive to focal heating and somatic activation is the pure result of a feed-forward damage propagation and integration, light-induced somatic Ca^{2+} transients clearly required IP_3-mediated mechanisms (Fig. 5), perhaps via the sensitization of IP_3Rs or the integration of Ca^{2+} activity from different astrocyte branches via Ca^{2+}-induced Ca^{2+} release mechanisms. In the cell periphery with its large membrane/cytosol ratio and tiny process volumes compared to the 2P focal volume (Fig. 1), other mechanisms seem to prevail. Candidates are channels with thermosensitive gating in the physiological temperature range like TRPV3 (54), STIM-1 (55), or a number of voltage-gated channels (56). Temperature variations around 37°C also sensitize to diverse stimuli triggering channel opening TRPV4 channels that are expressed in roughly 1/3 of astrocytes (57,58). Other Ca^{2+} influx pathways potentially targeted by NIR illumination are the plasma membrane sodium-calcium exchanger (NCX) and TRPM2 (59), the latter regulated by oxidative stress. Alternatively, heat-induced pore formation or lipid rearrangements and plasma membrane perforation and/or of the membranes of Ca^{2+} stores could mediate microdomain Ca^{2+} hyperactivity, but it would seem unlikely that this type of damage will result in the same stereotyped waveform of Ca^{2+} microdomain signals as in healthy cells. The origin and function of astrocyte Ca^{2+} microdomain signals rests enigmatic, and the detailed mechanistic investigation of the damage mechanism is beyond the scope of this work.

Finally, in as much as we conducted all our experiments at 31–34°C bath temperature (a common practice in slice electrophysiology), one might argue that laser-induced temperature gradients actually bring the recording temperature closer to physiological 37°C. Our observation of more frequent microdomain Ca^{2+} activity and the occurrence of somatic Ca^{2+} signals could then likely be physiological, and the quiet state is a result of the cell being too cold. Yet, even if this would be the case, because of the flying spot geometry, we are in a nonequilibrium situation, and the local heating will depend, in addition to the average power, on the recording depth and on scan parameters that influence local temperature gradients like the pixel dwell time, the spatial resolution, the use of flyback blanking, and the exact scan trajectory; this thermal-gradient nonequilibrium is not a recording condition in which physiologically meaningful data can be acquired. It will be interesting to investigate how different 2P geometries (single-spot sweeps versus resonant scanning, single-spot versus multispot geometries, raster scan versus random-access scanning, etc.) influence the result. Only the combined monitoring of the local temperature at the recording sites and 2P Ca^{2+} imaging can clarify this issue. Although future work will address this important question, one important conclusion we can already draw at this stage is that 2P Ca^{2+} imaging at tens of mW laser powers and with a single-spot geometry alters the tissue state and physiology under study.

Toward even shorter pulses

Our study illustrates the potential benefit of shorter pulses and lowering $\overline{P}$ for 2P excitation of GCaMP-based indicators at 920 nm and in the 100-fs regime. The 90-fs pulses used here were the minimum we could attain with our laser, microscope optics, the 20×/0.95w objective, and the precompensation optics at 920 nm. Even shorter pulses might be beneficial (60,61). This strategy will eventually be

bounded at some shortest tolerable pulse length because the resulting higher peak energies will in turn favor nonlinear photobleaching and photodamage pathways having a power exponent $m > 2$. The demonstration that phase-optimized 28-fs pulses reduced the bleaching rate of EGFP by a factor of four while maintaining the same intensity of the fluorescence signal (62) let us predict that there still might be some room for a further reduction of NIR-induced damage for brain imaging with even shorter pulses.

CONCLUSIONS

Overall, we conclude on a perspective similar to Icha et al. (49), who stated that "there are often subtler consequences of illumination that are imperceptible when only the morphology of samples is studied." Somatic astroglial Ca^{2+} signals in the absence of neuronal stimulation are a clear warning light for the onset of photodamage, and long before somatic transients are detectable, a heat-induced alteration of microdomain Ca^{2+} activity in the astrocyte periphery is observable. This transition from physiological to aberrant Ca^{2+} microdomain signals is more difficult to spot than the somatic hyperactivity, even when using a detailed analysis of several spike parameters. Our finding that pausing acquisitions can reverse the observed photoactivation indicates that reducing the light burden by all means, for example, a combination of shorter pulses, lower pulse rates, sparser "smarter" scan trajectories, and a lower duty cycle illumination alternating burst of imaging with dark episodes should be a promising strategy for maximizing the signal/damage ratio and permitting optical manipulation without compromising the physiology under study.

SUPPORTING MATERIAL

Supporting Material can be found online at https://doi.org/10.1016/j.bpj.2020.10.027.

AUTHOR CONTRIBUTIONS

E.S. and M.O. designed and performed research. E.S. analyzed the data. M.O. wrote the article.

ACKNOWLEDGMENTS

We thank Cendra Agulhon (Paris, France) for breeding the IP_3R2-KO mice used in this study and for help with immunofluorescence, Frank Pfrieger (Strasbourg, France) for providing the $GLASTcreER^{T2}$ mouse line, Marcel van't Hoff for LABVIEW programming, and Emmanuel Beaurepaire (Palaiseau, France), Erwin Neher (Göttingen, Germany), Stéphane Dieudonné (Paris, France), Manfred Lindau (Göttingen, Germany/Ithaca, NY), and many others for helpful discussions. Patrice Jegouzo, Christophe Tourain (workshop), and the animal house team around Claire Mader provided excellent technical assistance. We thank the late JacSue Kehoe (Paris, France) for carefully reading and commenting on an early version of this manuscript This article is dedicated to the memory of JacSue Kehoe (1935–2019), woman pioneer, colleague, and friend.

We were financed by the European Union (FP6-STRP "AUTO-SCREEN," FP7 ERA-NET NEURON "NANOSYN," FP7 JPND "SYNSPREAD," and H2020 EUROSTARS "OASIS"), the FranceBioImaging large-scale national infrastructure initiative (ANR-10-INSB-04, Investments for the future), and the Region Ile de France (Cancéropôle, "EDISON"). These funders had no role in study design, data collection and analysis, decision to publish, or preparation of the manuscript. The Oheim lab is a member of the *Ecole de Neurosciences de Paris* and the C'nano Ile de France excellence clusters for neurobiology and nanobiophotonics, respectively.

REFERENCES

1. Denk, W., J. H. Strickler, and W. W. Webb. 1990. Two-photon laser scanning fluorescence microscopy. *Science.* 248:73–76.
2. Stosiek, C., O. Garaschuk, …, A. Konnerth. 2003. In vivo two-photon calcium imaging of neuronal networks. *Proc. Natl. Acad. Sci. USA.* 100:7319–7324.
3. Helmchen, F., and W. Denk. 2005. Deep tissue two-photon microscopy. *Nat. Methods.* 2:932–940.
4. Svoboda, K., and R. Yasuda. 2006. Principles of two-photon excitation microscopy and its applications to neuroscience. *Neuron.* 50:823–839.
5. Mao, T., D. H. O'Connor, …, K. Svoboda. 2008. Characterization and subcellular targeting of GCaMP-type genetically-encoded calcium indicators. *PLoS One.* 3:e1796.
6. Looger, L. L., and O. Griesbeck. 2012. Genetically encoded neural activity indicators. *Curr. Opin. Neurobiol.* 22:18–23.
7. Akerboom, J., N. Carreras Calderón, …, L. L. Looger. 2013. Genetically encoded calcium indicators for multi-color neural activity imaging and combination with optogenetics. *Front. Mol. Neurosci.* 6:2.
8. Patterson, G. H., and D. W. Piston. 2000. Photobleaching in two-photon excitation microscopy. *Biophys. J.* 78:2159–2162.
9. Koester, H. J., D. Baur, …, S. W. Hell. 1999. Ca2+ fluorescence imaging with pico- and femtosecond two-photon excitation: signal and photodamage. *Biophys. J.* 77:2226–2236.
10. Hopt, A., and E. Neher. 2001. Highly nonlinear photodamage in two-photon fluorescence microscopy. *Biophys. J.* 80:2029–2036.
11. Tan, Y. P., I. Llano, …, E. Neher. 1999. Fast scanning and efficient photodetection in a simple two-photon microscope. *J. Neurosci. Methods.* 92:123–135.
12. Weisenburger, S., R. Prevedel, and A. Vaziri. 2017. Quantitative evaluation of two-photon calcium imaging modalities for high-speed volumetric calcium imaging in scattering brain tissue. *bioRxiv* https://doi.org/10.1101/115659.
13. Madisen, L., A. R. Garner, …, H. Zeng. 2015. Transgenic mice for intersectional targeting of neural sensors and effectors with high specificity and performance. *Neuron.* 85:942–958.
14. Slezak, M., C. Göritz, …, F. W. Pfrieger. 2007. Transgenic mice for conditional gene manipulation in astroglial cells. *Glia.* 55:1565–1576.
15. Petravicz, J., K. M. Boyt, and K. D. McCarthy. 2014. Astrocyte IP3R2-dependent Ca(2+) signaling is not a major modulator of neuronal pathways governing behavior. *Front. Behav. Neurosci.* 8:384.
16. Cesana, E., K. Pietrajtis, …, L. Forti. 2013. Granule cell ascending axon excitatory synapses onto Golgi cells implement a potent feedback circuit in the cerebellar granular layer. *J. Neurosci.* 33:12430–12446.
17. Ducros, M., M. van 't Hoff, …, M. Oheim. 2011. Efficient large core fiber-based detection for multi-channel two-photon fluorescence microscopy and spectral unmixing. *J. Neurosci. Methods.* 198:172–180.
18. Oheim, M., E. Beaurepaire, …, S. Charpak. 2001. Two-photon microscopy in brain tissue: parameters influencing the imaging depth. *J. Neurosci. Methods.* 111:29–37.
19. Schneider, C. A., W. S. Rasband, and K. W. Eliceiri. 2012. NIH Image to ImageJ: 25 years of image analysis. *Nat. Methods.* 9:671–675.

20. Rueden, C. T., J. Schindelin, …, K. W. Eliceiri. 2017. ImageJ2: ImageJ for the next generation of scientific image data. *BMC Bioinformatics.* 18:529.
21. Schindelin, J., I. Arganda-Carreras, …, A. Cardona. 2012. Fiji: an open-source platform for biological-image analysis. *Nat. Methods.* 9:676–682.
22. Bethge, P., S. Carta, …, F. Helmchen. 2017. An R-CaMP1.07 reporter mouse for cell-type-specific expression of a sensitive red fluorescent calcium indicator. *PLoS One.* 12:e0179460.
23. Ohkura, M., T. Sasaki, …, J. Nakai. 2012. Genetically encoded green fluorescent Ca2+ indicators with improved detectability for neuronal Ca2+ signals. *PLoS One.* 7:e51286.
24. Shigetomi, E., S. Kracun, …, B. S. Khakh. 2010. A genetically targeted optical sensor to monitor calcium signals in astrocyte processes. *Nat. Neurosci.* 13:759–766.
25. Haustein, M. D., S. Kracun, …, B. S. Khakh. 2014. Conditions and constraints for astrocyte calcium signaling in the hippocampal mossy fiber pathway. *Neuron.* 82:413–429.
26. Rungta, R. L., L. P. Bernier, …, B. A. MacVicar. 2016. Ca^{2+} transients in astrocyte fine processes occur via Ca^{2+} influx in the adult mouse hippocampus. *Glia.* 64:2093–2103.
27. Bindocci, E., I. Savtchouk, …, A. Volterra. 2017. Three-dimensional Ca^{2+} imaging advances understanding of astrocyte biology. *Science.* 356:eaai8185.
28. Tian, L., S. A. Hires, …, L. L. Looger. 2009. Imaging neural activity in worms, flies and mice with improved GCaMP calcium indicators. *Nat. Methods.* 6:875–881.
29. Ye, L., M. A. Haroon, …, M. Paukert. 2017. Comparison of GCaMP3 and GCaMP6f for studying astrocyte Ca2+ dynamics in the awake mouse brain. *PLoS One.* 12:e0181113.
30. König, K., T. W. Becker, …, K. J. Halbhuber. 1999. Pulse-length dependence of cellular response to intense near-infrared laser pulses in multiphoton microscopes. *Opt. Lett.* 24:113–115.
31. Podgorski, K., and G. Ranganathan. 2016. Brain heating induced by near-infrared lasers during multiphoton microscopy. *J. Neurophysiol.* 116:1012–1023.
32. Débarre, D., N. Olivier, …, E. Beaurepaire. 2014. Mitigating phototoxicity during multiphoton microscopy of live Drosophila embryos in the 1.0-1.2 µm wavelength range. *PLoS One.* 9:e104250.
33. Schönle, A., and S. W. Hell. 1998. Heating by absorption in the focus of an objective lens. *Opt. Lett.* 23:325–327.
34. Bánsághi, S., T. Golenár, …, G. Hajnóczky. 2014. Isoform- and species-specific control of inositol 1,4,5-trisphosphate (IP3) receptors by reactive oxygen species. *J. Biol. Chem.* 289:8170–8181.
35. Agarwal, A., P.-H. Wu, …, D. E. Bergles. 2017. Transient opening of the mitochondrial permeability transition pore induces microdomain calcium transients in astrocyte processes. *Neuron.* 93:587–605.e7.
36. Sherwood, M. W., M. Arizono, …, K. Mikoshiba. 2017. Astrocytic IP_3 Rs: contribution to Ca^{2+} signalling and hippocampal LTP. *Glia.* 65:502–513.
37. Srinivasan, R., B. S. Huang, …, B. S. Khakh. 2015. Ca(2+) signaling in astrocytes from Ip3r2(-/-) mice in brain slices and during startle responses in vivo. *Nat. Neurosci.* 18:708–717.
38. Sheppard, C. J., and R. Kompfner. 1978. Resonant scanning optical microscope. *Appl. Opt.* 17:2879–2882.
39. Macias-Romero, C., V. Zubkovs, …, S. Roke. 2016. Wide-field medium-repetition-rate multiphoton microscopy reduces photodamage of living cells. *Biomed. Opt. Express.* 7:1458–1467.
40. Liu, Y., G. J. Sonek, …, B. J. Tromberg. 1996. Physiological monitoring of optically trapped cells: assessing the effects of confinement by 1064-nm laser tweezers using microfluorometry. *Biophys. J.* 71:2158–2167.
41. Peterman, E. J., F. Gittes, and C. F. Schmidt. 2003. Laser-induced heating in optical traps. *Biophys. J.* 84:1308–1316.
42. Picot, A., S. Dominguez, …, V. Emiliani. 2018. Temperature rise under two-photon optogenetic brain stimulation. *Cell Rep.* 24:1243–1253.e5.
43. Sun, M.-Y., P. Devaraju, …, T. A. Fiacco. 2014. Astrocyte calcium microdomains are inhibited by bafilomycin A1 and cannot be replicated by low-level Schaffer collateral stimulation in situ. *Cell Calcium.* 55:1–16.
44. Kalmbach, A. S., and J. Waters. 2012. Brain surface temperature under a craniotomy. *J. Neurophysiol.* 108:3138–3146.
45. Chen, X., U. Leischner, …, A. Konnerth. 2012. LOTOS-based two-photon calcium imaging of dendritic spines in vivo. *Nat. Protoc.* 7:1818–1829.
46. Iyer, V., T. M. Hoogland, and P. Saggau. 2006. Fast functional imaging of single neurons using random-access multiphoton (RAMP) microscopy. *J. Neurophysiol.* 95:535–545.
47. Salomé, R., Y. Kremer, …, L. Bourdieu. 2006. Ultrafast random-access scanning in two-photon microscopy using acousto-optic deflectors. *J. Neurosci. Methods.* 154:161–174.
48. Duemani Reddy, G., K. Kelleher, …, P. Saggau. 2008. Three-dimensional random access multiphoton microscopy for functional imaging of neuronal activity. *Nat. Neurosci.* 11:713–720.
49. Icha, J., M. Weber, …, C. Norden. 2017. Phototoxicity in live fluorescence microscopy, and how to avoid it. *BioEssays.* 39.
50. Horton, N. G., K. Wang, …, C. Xu. 2013. *In vivo* three-photon microscopy of subcortical structures within an intact mouse brain. *Nat. Photonics.* 7:205–209.
51. Guesmi, K., L. Abdeladim, …, F. Druon. 2018. Dual-color deep-tissue three-photon microscopy with a multiband infrared laser. *Light Sci. Appl.* 7:12.
52. Nett, W. J., S. H. Oloff, and K. D. McCarthy. 2002. Hippocampal astrocytes in situ exhibit calcium oscillations that occur independent of neuronal activity. *J. Neurophysiol.* 87:528–537.
53. Wang, X., N. Lou, …, M. Nedergaard. 2006. Astrocytic Ca2+ signaling evoked by sensory stimulation in vivo. *Nat. Neurosci.* 9:816–823.
54. Xu, H., I. S. Ramsey, …, D. E. Clapham. 2002. TRPV3 is a calcium-permeable temperature-sensitive cation channel. *Nature.* 418:181–186.
55. Xiao, B., B. Coste, …, A. Patapoutian. 2011. Temperature-dependent STIM1 activation induces Ca^{2}+ influx and modulates gene expression. *Nat. Chem. Biol.* 7:351–358.
56. Chowdhury, S., B. W. Jarecki, and B. Chanda. 2014. A molecular framework for temperature-dependent gating of ion channels. *Cell.* 158:1148–1158.
57. Shibasaki, K., K. Ikenaka, …, Y. Ishizaki. 2014. A novel subtype of astrocytes expressing TRPV4 (transient receptor potential vanilloid 4) regulates neuronal excitability via release of gliotransmitters. *J. Biol. Chem.* 289:14470–14480.
58. Gao, X., L. Wu, and R. G. O'Neil. 2003. Temperature-modulated diversity of TRPV4 channel gating: activation by physical stresses and phorbol ester derivatives through protein kinase C-dependent and -independent pathways. *J. Biol. Chem.* 278:27129–27137.
59. Kühn, F. J., I. Heiner, and A. Lückhoff. 2005. TRPM2: a calcium influx pathway regulated by oxidative stress and the novel second messenger ADP-ribose. *Pflugers Arch.* 451:212–219.
60. Xi, P., Y. Andegeko, …, M. Dantus. 2008. Greater signal, increased depth, and less photobleaching in two-photon microscopy with 10 fs pulses. *Opt. Commun.* 281:1841–1849.
61. Pang, S., A. T. Yeh, …, K. E. Meissner. 2009. Beyond the 1/Tp limit: two-photon-excited fluorescence using pulses as short as sub-10-fs. *J. Biomed. Opt.* 14:054041.
62. Kawano, H., Y. Nabekawa, …, K. Midorikawa. 2003. Attenuation of photobleaching in two-photon excitation fluorescence from green fluorescent protein with shaped excitation pulses. *Biochem. Biophys. Res. Commun.* 311:592–596.

Biophysical Journal, Volume *119*

Supplemental Information

Infrared Excitation Induces Heating and Calcium Microdomain Hyperactivity in Cortical Astrocytes

Elke Schmidt and Martin Oheim

Supplementary Information

Pulse-length effects in 2P-micoscopy. I. Infrared excitation induces brain heating and calcium microdomain hyper-activity in cortical astrocytes

Elke Schmidt[a] and Martin Oheim[a *, ✉]

[a]Université de Paris, SPPIN – Saints Pères Paris Institute for the Neurosciences, CNRS, Paris, F-75006 France.

*ORCID id: orcid.org/0000-0001-8139-167X

✉ martin.oheim@parisdescartes.fr

This PDF file includes:

Supplementary text
Figs. S1 to S6
Table S1
Captions for movies S1 to S2
References for SI reference citations

Other supplementary materials for this manuscript include the following:

Movies S1 to S2

SUPPLEMENTARY TEXT

List of abbreviations

2P	-	two-photon
4-OH	-	4-hydroxy (-tamoxifen)
ACSF	-	artificial cerebrospinal fluid
AOM	-	acousto-optical modulator
a.u.	-	arbitrary units
Ca^{2+}	-	calcium
CNRS	-	*Centre National de la Recherche Scientifique*
DAPI	-	4',6-Diamidine-2'-phenylindole dihydrochloride
EU	-	European Union
GDD	-	group delay dispersion
i.p.	-	intraperitoneally
IP_3R2	-	inositol 1,4,5-trisphosphate receptor subtype2
GUI	-	graphical user interface
KO	-	knock-out
OCT	-	optimal cutting temperature
OD	-	optical density
PBS	-	phosphate buffered saline
PCR	-	polymerase chain reaction
PFA	-	paraformaldehyde
ROI	-	region of interest
SD	-	standard deviation
SEM	-	standard error of the mean

SUPPLEMENTAL ONLINE METHODS

Drugs and reagents

Unless otherwise stated, reagents were purchased from Sigma Aldrich (Deisenhofen, Germany).

Immunofluorescence

Mice were anesthetized with pentobarbital, injected *i.p*. (150 mg/kg body weight), perfused with 4% paraformaldehyde (PFA) in 0.02M phosphate buffered saline (PBS) and their brains were removed, postfixed in PFA (2h, 4%) and cryoprotected in 20% sucrose in 0.02 M PBS overnight. Tissue was frozen in Optimal Cutting Temperature (OCT) compound (Sakura Finetek Europe, Leiden, Netherlands) at -30° for cutting 16-µm sections with a cryostat. Sections were stored at -80°C prior to use. For immunofluorescence, slides were defrosted, washed 2× 15 min in 0.02 M PBS, and incubated overnight with primary antibodies (see Table S1) diluted in 0.02 M PBS, 0.02% Na-azide, 0.3 M Triton X-100 at room temperature (RT, 20-23°C) in a humid chamber. The day after, slides were washed 4× 15 min in 0.02M PBS, and incubated 2h with the secondary antibody diluted in 0.02 M PBS, 0.02% Na-azide, 0.3M Triton X-100 (see Table S1). Finally, slides were washed 2× in PBS (15 min, 0.02 M), mounted with Vectashield (containing DAPI, Vector Laboratories, Burlingame CA, USA), and sealed with coverslips. Slices incubated with secondary antibodies only were used as negative controls to set parameters for antibody-specific fluorescence image acquisition in each experiment. Images were acquired in epifluorescence (Axio Observer Z1, ZEISS, Oberkochen, Germany) fitted with a PlanNeoFluar ×20/0.5-NA objective, a COLIBRI-2 4-LED light-source (365 nm, 470 nm, 590 nm, 625 nm) and matched ZEISS filter cubes (see details in Table S1). Identical acquisition settings were used for the negative controls and experimental slides.

SUPPLEMENTARY FIGURES

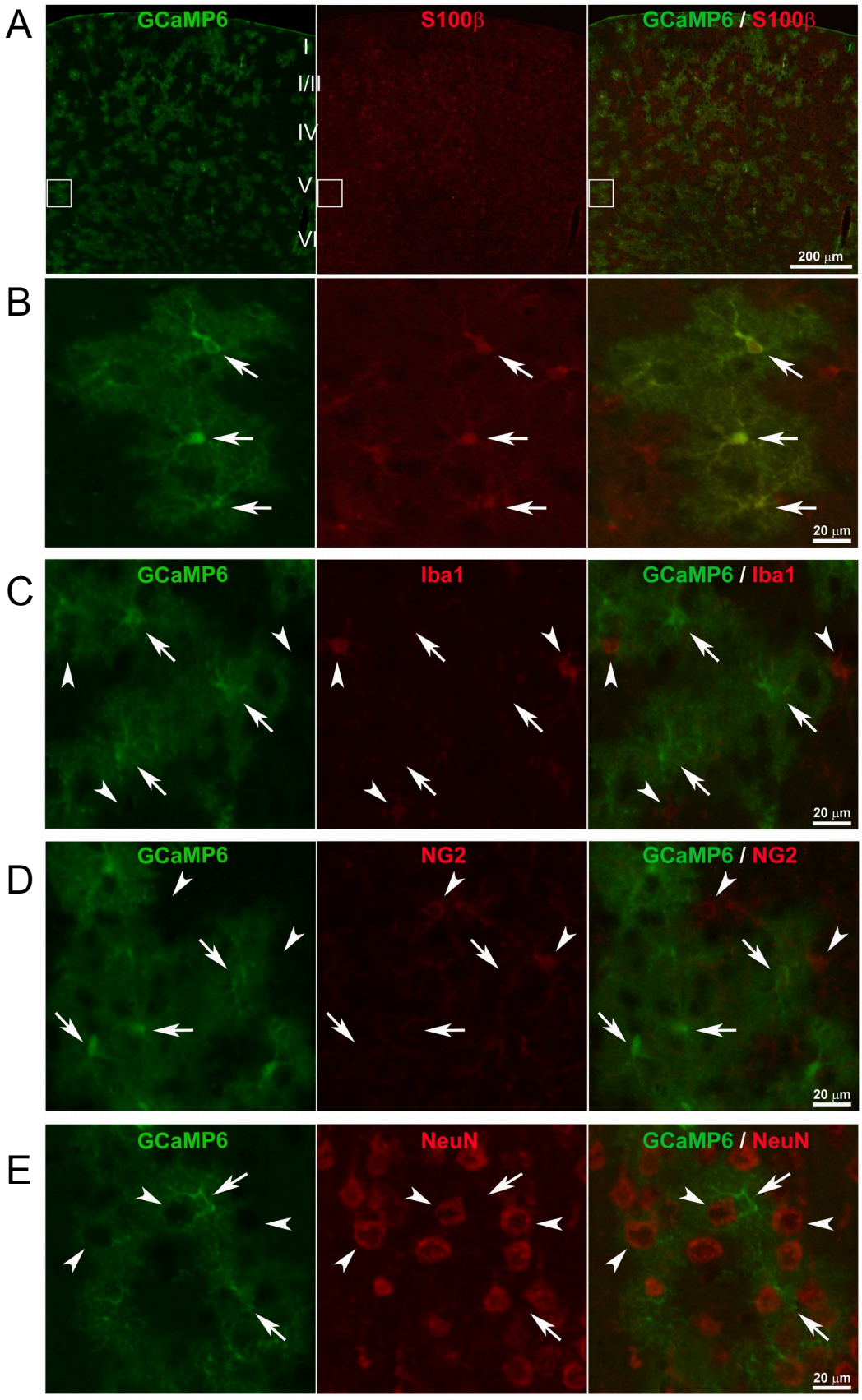

Fig. S1. GLAST-driven GCaMP6f expression is astrocyte-specific.

Immunofluorescence imaging of slices from GLAST-CreER^{T2}::GCaMP6f mice. (*A*) Throughout layers I-VI of the somatosensory cortex of 4-OH tamoxifen-injected mice, the genetically encoded Ca^{2+} indicator GCaMP6f (*top*, *left*) was selectively expressed in S100β-positive astrocytes (*top*, *middle*). Some 42% of S100β^{+} astrocytes expressed GCaMP6f and 99% of GCaMP6f^{+} cells expressed S100β. (*B*) Pseudo-color red-green overlap (*right*) at the single-cell level (*arrows* mark astrocyte cell bodies) when zooming in on the boxed region in (A). GCaMP6f is neither expressed in Iba1-positive microglia (C, *arrowheads*) nor in NG2-expressing oligodendrocyte precursor cells (D), and only marginal expression is detected in NeuN-positive neurons (<0.05%, panel E). Scale bars: 200 and 20 μm, respectively, as shown on the rightmost panel.

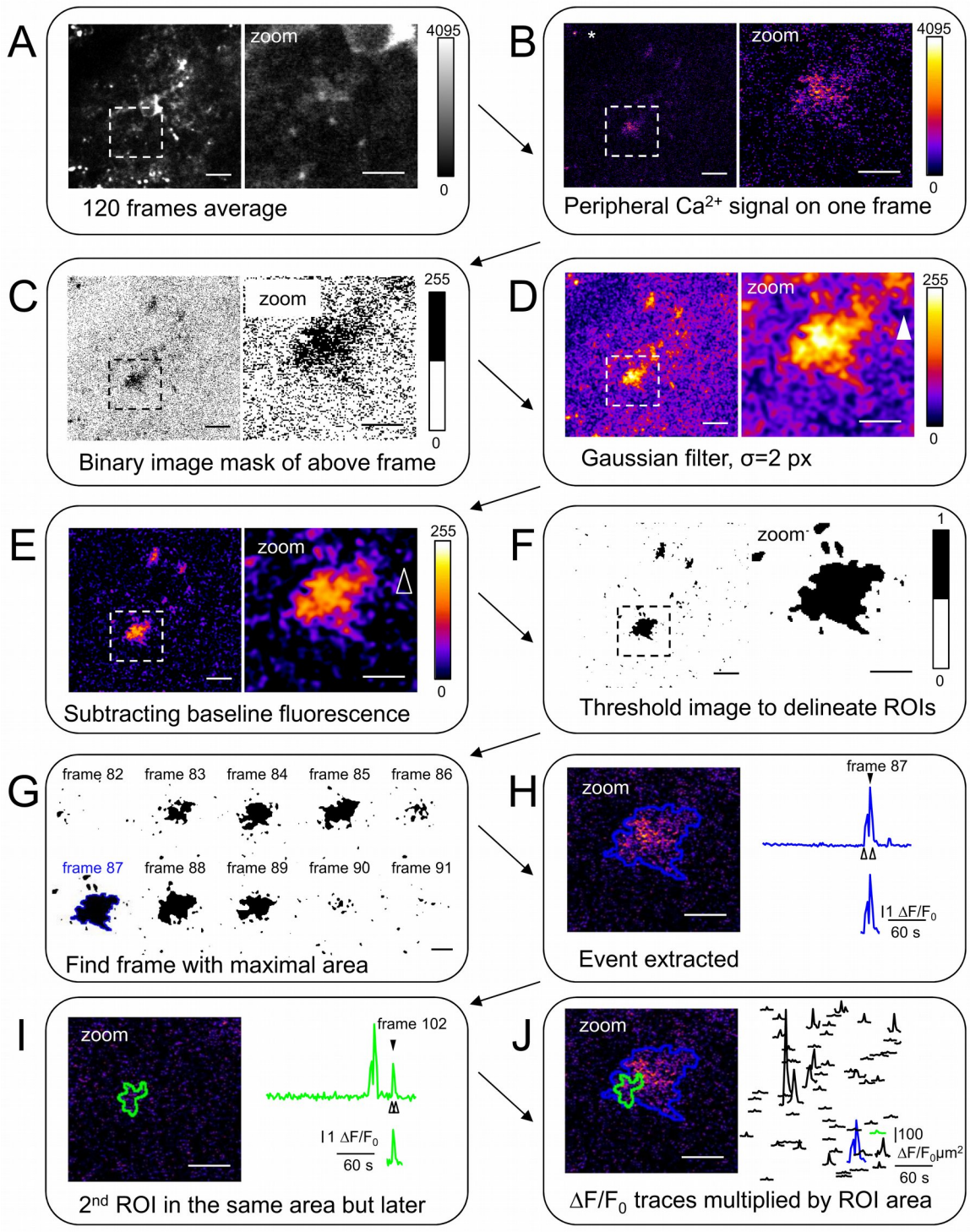

Fig.S2 ImageJ and IGOR routine for ROI- and event-detection. Steps of semi-auto-mated detection of Ca^{2+} transients in astrocyte processes. (*A*) Time-average of an 2P-fluorescence image series (0.5 Hz, 120 frames) recorded in a GLAST-creER^{T2}:ROSA-CAG-LSL-GCaMP6f mouse. Scale

bar, 10 µm. *Right*, zoomed view of the boxed region. Scale bar, 5 µm. Grey-values are photomultiplier counts. We systematically used such projections along the temporal axis to better appreciate the fine cell morphology. For the region shown, a localized, spontaneous Ca^{2+} transient occurred on frame 87. The fluorescence on the top right corner of the zoomed image corresponds to the baseline fluorescence of the soma. (B) shows the Ca^{2+} event detected on frame 87 and its zoom on a 'fire' LUT, illustrating the difficulty to outline regions of interest by simpler procedures. The asterisk shows an artifacts in the form bright and almost stationary auto-fluorescent spots resulting from lipofuscin-rich granules (10). (*C*) After baseline and outlier removal (see Methods for details), all pixels > 255 were set to 1 to prepare for the Gaussian filtering (see Methods for explanations). (*D*) In the next step, the image stack was filtered with a Gaussian filter (σ=2 pixel). Note the high baseline fluorescence of the soma (solid arrowhead). (*E*) As next step, the difference in baseline fluorescence, which makes it difficult to distinguish between Ca^{2+} events and structures with higher baseline fluorescence, was removed by subtracting the average of the first 10 frames. Note that the baseline fluorescence of the soma in the right upper corner of the zoom image (open arrowhead) disappears. (*F*) Then, a binary image was created by setting as a threshold the mean intensity of all pixels >0 of the first 10 frames plus 3 times its SD. The ROIs are delineated (area > 3 µm²). (*G*) If the Ca^{2+} event extents over several frames, only the ROI outline on the frame where the signal has its biggest area is retained (for details see online methods). In this example the Ca^{2+} signal is detectable from frame 83-89 and the ROI detected on frame 87 has the biggest area. (*H*) The mean intensity over time is extracted from the original stack (that had been processed for background and outlier removal) and normalized. The corresponding $\Delta F/F_0(t)$ trace (shown in blue) shows two Ca^{2+} peaks. However, only the 1st peak (black arrowhead) corresponds to the Ca^{2+} event detected on frame 87. The 2nd peak on the blue trace corresponds to a 2nd, spatially overlapping, Ca^{2+} event the ROI of which (shown in green) was detected on frame 102. (*I*) The $\Delta F/F_0(t)$ trace of the second, overlapping ROI (shown in green) also shows both Ca^{2+} peaks. If we would show the full-length of all $\Delta F/F_0(t)$ traces as independent traces, we would therefore count the same Ca^{2+} peak two times (or even multiple times if more than two ROIs are overlapping). Therefore, the $\Delta F/F_0$ trace was cut before and after the Ca^{2+} peak corresponding to the ROI. (*J*) When looking at the extracted the $\Delta F/F_0$ traces of an ROI, the information of the spatial extent of the Ca^{2+} event is lost. Therefore, all $\Delta F/F_0$ traces were weighed with their respective ROI's area size. For display, the $\Delta F/F_0(t)$ peaks were ordered by their (increasing) distance to the soma.

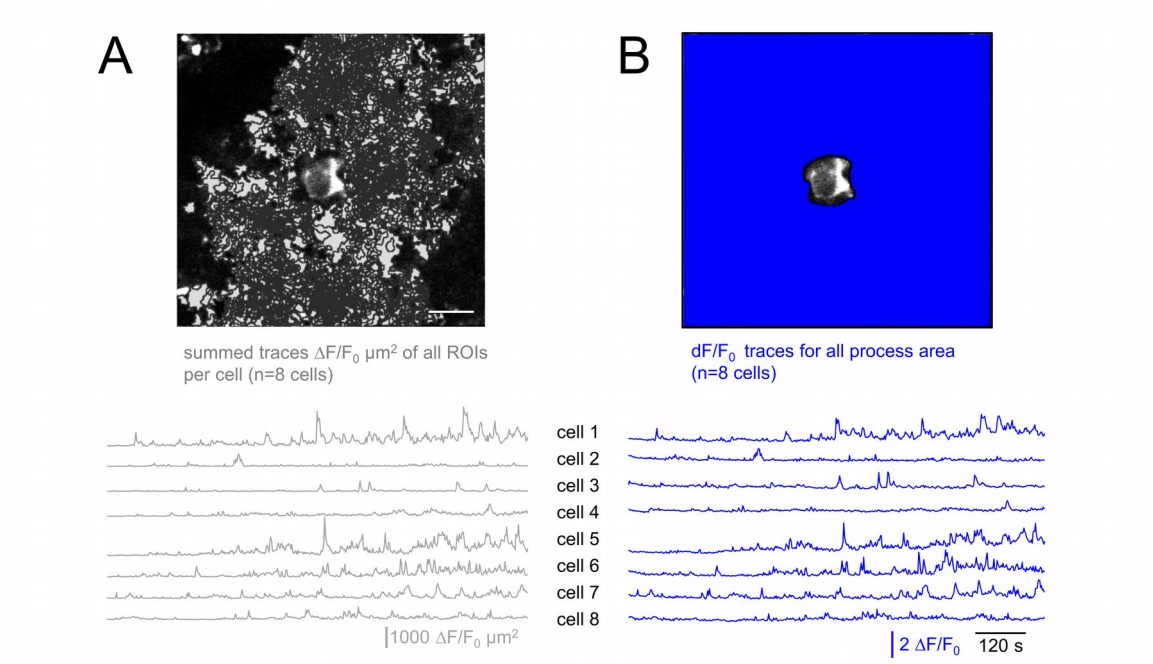

Fig. S3. Summed activity built from cumulating the weighted individually detected ROIs is equivalent to the integrated activity measured from a single large region encompassing the entire neuropil. (A) *Top*, all detected ROIs during a 500-frame recording, superimposed on the morphological overview (as in Fig. 1A) of the same cell as shown in Fig. 1 and Fig. 2. The summed activity trace is the sum of the $\Delta F/F_0(t)$ transients detected in the area of the processes (excluding the soma), multiplied, for each event, with the ROI size. Note that even if the entire cell is covered by overlaying ROIs, each ROI represents one peak at a given time, and that

asynchronous activity has been added up on the 'summed activity trace'. (c.f., Fig.1, Fig.S2 and Methods). *Bottom*, the summed activity of the cell shown above (cell 1), as well as of the other seven cells from this data set. (*B*) *Top*, the alternative, much simpler 'center-versus-surround' analysis lumps the entire process region together to one big ROI (blue). *Bottom*, the thus generated $\Delta F/F_0$ traces for the same cells as in (A) are very similar to the summed activity traces built from detected events scaled with their respective ROI size. Thus, the summed activity traces are a valid way for quantifying the overall Ca^{2+}-activity (and activation). On the other hand, at least at the signal-to-noise ratio and low background in our experiments, the much simpler centre-vs.-surround analysis is a good proxy for the ROI-based analysis, when only cumulative effects shall be studied. Scale bar, 10µm

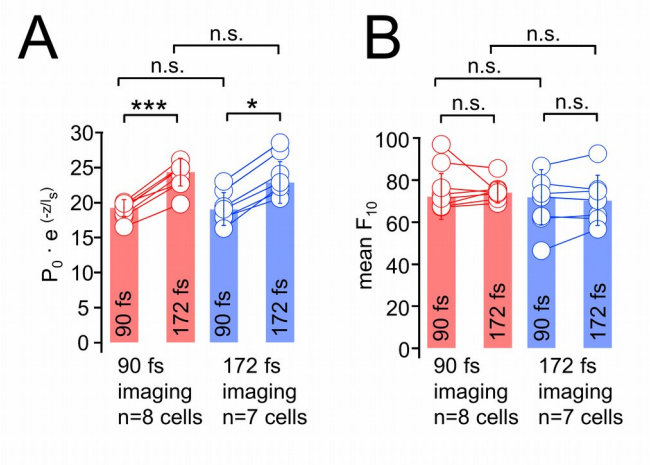

Fig. S4. Shorter pulses allow lowering the average power. (*A*) Laser powers used for 2P imaging, scaled with the imaging depth, for all cells shown in Fig. 3. Prior to imaging cells with either 90- or 172-fs pulses, we recorded 'ministacks' of ten frames with each pulse length and the average laser power was adjusted for constant 2P fluorescence (i.e., $\overline{P}^2/\tau = const.$). The power required for achieving an equal signal with 172-fs pulses was significantly higher (two sided nonparametric Wilcoxon-Mann-Whitney two-sample rank test) than for 90 fs, and there was no significant difference between the adjustment of the average laser power for both conditions (if cells were imaged with 90- or 172-fs pulses in the following recording), which means that $\overline{P}$ had been adjusted correctly. On average, we needed to increase by a factor of 1.26 ± 0.06 $\overline{P}$ when going from 90- to 172-fs pulses. (*B*) Indistinguishable baseline GCaMP6f-fluorescence measured in manually selected cell ROIs on 10-image ministacks. Bar graphs show median ± SD; *: $P < 0.05$, **: $P < 0.01$, ***: $P < 0.005$, n.s.: not significant.

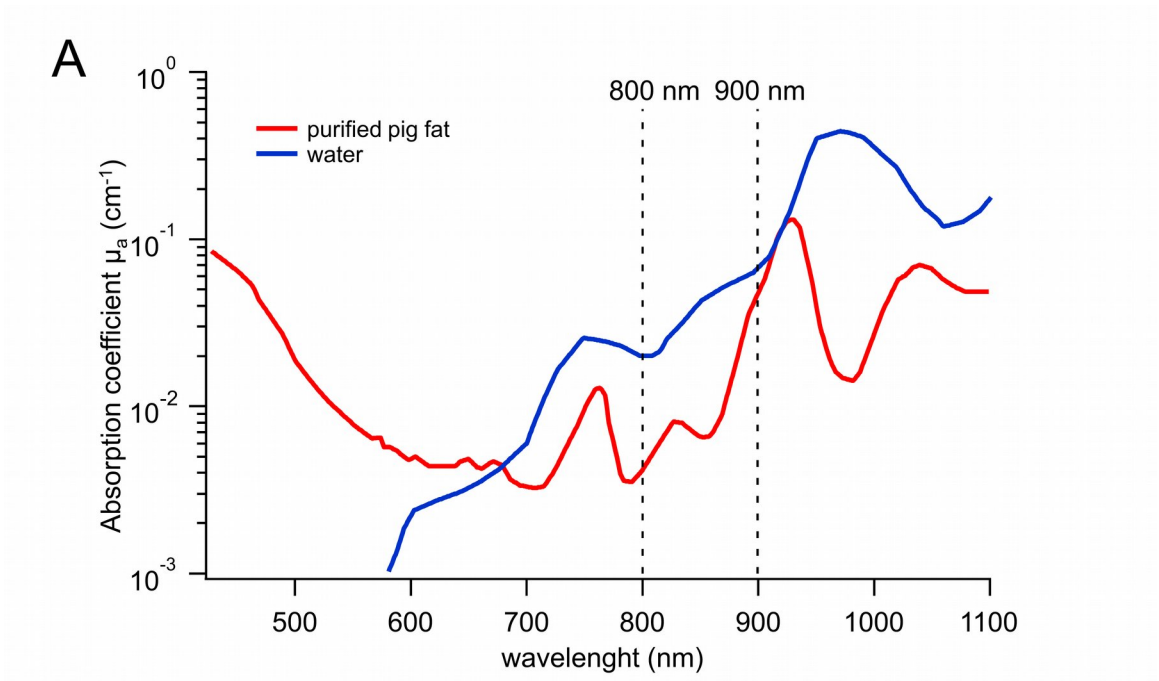

Fig. S5 Water and lipid absorption increase by more than one order of magnitude between 800 and 900 nm. Log plot of absorption coefficient μ_a vs. wavelength λ. μ_a for water (*blue*) and lipid (*red*), the main components of brain tissue, increase by more than one order of magnitude between λ < 800 nm (which have been typically been used for small-molecule chemical indicators) and λ > 900 nm, as now commonly used for imaging GECIs and light-activation of optogenetic actuators. Data from (11) (purified pig fat) and (12) (water)

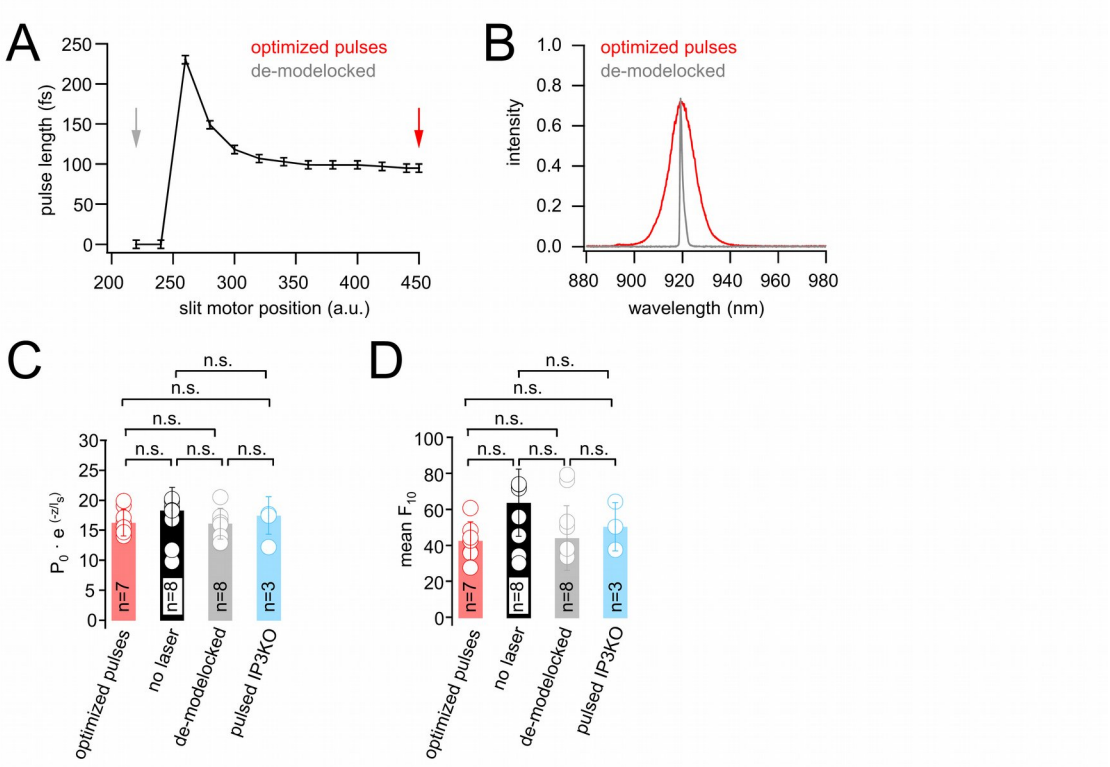

Fig. S6. CW-operation of the MaiTai laser. For de-modelocking a motorized slit aperture inside the laser cavity is partially closed under software control. (A), pulse lengths measured by autocorrelation (± 5 fs measurement error), as a function of slit motor position in arbitrary units (a.u., see Online Methods sections for details). The slit position is an internal measurement of the laser and the resulting slit diameter will differ for every laser. In our case, at 920 nm, 450 a.u. correspond to the slit motor position during normal fs-pulsed operation. For values below 350 a.u., the measured pulse length gradually increased and the laser stopped pulsing for motor positions <240 a.u.. We performed our CW experiments with a motor position of 220 a.u. (B), as expected, de-modelocking results in a reduction of the spectral width of the laser output (*red*, pulse spectrum at 90 fs; *grey*, spectrum after de-modelocking). Because only one of the blades of the slit aperture moves, the wavelength spectrum resulting when narrowing the slit is not exactly symmetrical, and the center wavelength of the pulse does not correspond to the preset command wavelength. Hence, after de-modelocking, a command wavelength of 933 nm is

necessary for a laser output centered at 920 nm. (C), Laser powers used for 2PEF imaging (normalized with the exponential power loss for imaging depth for all cells represented in Fig. 4 and Fig. 5). There is no significant difference between any of the four experimental conditions (two sided nonparametric Wilcoxon-Mann-Whitney two-sample rank test and non-parametric Kruskal-Wallis group test). (D), mean baseline fluorescence of first ten image frames is indistinguishable. Bar graphs show median ± SD; *: $P < 0.05$, **: $P < 0.01$, ***: $P < 0.005$, n.s.: not significant.

Table S1.

Antibodies, dilutions, wavelengths and filters used for immunofluorescence.

Primary antibodies	*dilution*	*species*	*supplier*	*reference*	-				
Anti-GFP	1/500	chicken	Novus-Biologicals	NB600-308	-				
Anti-S100°	1/500	rabbit	Abcam	AB52642	-				
Anti-Iba1	1/500	rabbit	Wako/Sobodia	AB5320	-				
Anti-NG2	1/500	rabbit	Millipore	019-19741	-				
Anti-NeuN	1/500	guinea pig	Millipore	ABN900	-				
Secondary antibodies					*ex*	*dic*	*em*	ZEISS set	*ref*
Anti-chicken-AlexaFluor488	1/1000	goat	Invitrogen	A-11039	BP470/40	FT495	BP525/50	eGFP shift free (HE)	38
Anti-guinea-pig-AlexaFluor546	1/1000	goat	Invitrogen	A-11074	BP545/25	FT570	BP605/70	Cy3 shift free (E)	43
Anti-rabbit-AlexaFluor546	1/1000	goat	Invitrogen	A-11035	BP545/25	FT570	BP605/70	Cy3 shift free (E)	43
DAPI					G365	FT395	BP445/50	DAPI shift free	49

Movie S1. *Spontaneous Ca^{2+} signals in a murine cortical astrocyte expressing GCaMP6f*

Diffraction-limited two-photon imaging at 0.5 Hz of an astrocyte expressing GCaMP6f in the S1 barrel cortex of an acute mouse brain slice. Analysis of this cell is shown in Fig. 1 and Fig. 2A Highly localized, spontaneous, asynchronous microdomain Ca^{2+}-signals can be seen throughout the entire neuropil. The raw-data has only been median filtered (0.5 px) after background and outlier removal (as described in the Online Methods section) and is displayed using a "fire" lookup table (LUT). The movie is superimposed on the time-averaged fluorescence (shown in grey value) over the 1st 120 frames to have visual morphological landmarks. The movie shows a 4-min recording at 25 fps (i.e., 50 times faster than original). Scale bar, 10 µm.

Movie S2. *Increase of spontaneous astrocytic Ca^{2+} signals during 2PEF imaging*

Diffraction-limited two-photon imaging at 0.5 Hz of an astrocyte expressing GCaMP6f in the S1 barrel cortex of an acute mouse brain slice as in Movie 1, but with much longer recording time (16.3 min, 500 frames). With increasing recording time, the microdomain Ca^{2+} activity in the fine processes is increasing in frequency, and an aberrant activity of the otherwise silent soma can been seen towards the end of the recording. The original data has been median filtered (0.5 px) after background and outlier removal (as described in the Online Methods section) and is shown with a "fire" LUT superimposed with a morphological image obtained by averaging the 1st 120 frames (grey scale LUT). This cell is corresponding to the one shown in the raster plot in Fig. 3A. The movie is shown at 25 fps (i.e., 50-times faster than the original). Scale bar, 10 µm.

Supplementary references

1. Denk W, Strickler JH, & Webb WW (1990) Two-photon laser scanning fluorescence microscopy. *Science* 248(4951):73-76.
2. Stosiek C, Garaschuk O, Holthoff K, & Konnerth A (2003) In vivo two-photon calcium imaging of neuronal networks. *Proc. Natl. Acad. Sci. USA* 100(12):7319-7324.
3. Helmchen F & Denk W (2005) Deep tissue two-photon microscopy. *Nat. Methods* 2(12):932-940.
4. Svoboda K & Yasuda R (2006) Principles of two-photon excitation microscopy and its applications to neuroscience. *Neuron* 50(6):823-839.
5. Mao T, O'Connor DH, Scheuss V, Nakai J, & Svoboda K (2008) Characterization and subcellular targeting of GCaMP-type genetically-encoded calcium indicators. *PloS One* 3(3):e1796.
6. Looger LL & Griesbeck O (2012) Genetically encoded neural activity indicators. *Curr. Op. Neurobiol.* 22(1):18-23.
7. Akerboom J, *et al.* (2013) Genetically encoded calcium indicators for multi-color neural activity imaging and combination with optogenetics. *Front. Mol. Neurosci.* 6.
8. Patterson GH & Piston DW (2000) Photobleaching in two-photon excitation microscopy. *Biophys. J.* 78(4):2159-2162.

9. Koester HJ, Baur D, Uhl R, & Hell SW (1999) Ca 2+ fluorescence imaging with pico-and femtosecond two-photon excitation: signal and photodamage. *Biophys. J.* 77(4):2226-2236.
10. Hopt A & Neher E (2001) Highly nonlinear photodamage in two-photon fluorescence microscopy. *Biophys. J.* 80(4):2029-2036.
11. Tan Y, Llano I, Hopt A, Würriehausen F, & Neher E (1999) Fast scanning and efficient photodetection in a simple two-photon microscope. *J. Neurosci. Meth.* 92(1):123-135.
12. Weisenburger S, Prevedel R, & Vaziri A (2017) Quantitative evaluation of two-photon calcium imaging modalities for high-speed volumetric calcium imaging in scattering brain tissue. *bioRxiv*:115659.
13. Ohkura M*, et al.* (2012) Genetically encoded green fluorescent Ca2+ indicators with improved detectability for neuronal Ca2+ signals. *PloS one* 7(12):e51286.
14. Shigetomi E, Kracun S, Sofroniew MV, & Khakh BS (2010) A genetically targeted optical sensor to monitor calcium signals in astrocyte processes. *Nat. Neurosci.* 13(6):759-766.
15. Haustein MD*, et al.* (2014) Conditions and constraints for astrocyte calcium signaling in the hippocampal mossy fiber pathway. *Neuron* 82(2):413-429.
16. Rungta RL*, et al.* (2016) Ca2+ transients in astrocyte fine processes occur via Ca2+ influx in the adult mouse hippocampus. *Glia* 64(12):2093-2103.
17. Bindocci E*, et al.* (2017) Three-dimensional Ca2+ imaging advances understanding of astrocyte biology. *Science* 356(6339):eaai8185.
18. Tian L*, et al.* (2009) Imaging neural activity in worms, flies and mice with improved GCaMP calcium indicators. *Nature Meth* 6(12):875-881.
19. Ye L, Haroon MA, Salinas A, & Paukert M (2017) Comparison of GCaMP3 and GCaMP6f for studying astrocyte Ca2+ dynamics in the awake mouse brain. *PloS One* 12(7):e0181113.
20. König K, Becker TW, I. F, Riemann I, & Halbhuber KJ (1999) Pulse-length dependence of cellular response to intense near-infrared pulses in multiphoton microscopes. *Opt. Lett.* 24:113-115.
21. Podgorski K & Ranganathan G (2016) Brain heating induced by near-infrared lasers during multiphoton microscopy. *J. Neurophysiol.* 116:1012-1023.
22. Debarre D, Olivier N, Supatto W, & Beaurepaire E (2014) Mitigating phototoxicity during multiphoton microscopy of live Drosophila embryos in the 1.0–1.2 μm wavelength range. *PLoS One* 9(8):e104250.
23. Schönle A & Hell SW (1998) Heating by absorption in the focus of an objective lens. *Opt. Lett.* 23(5):325-327.
24. Bánsághi S*, et al.* (2014) Isoform-and species-specific control of inositol 1, 4, 5-trisphosphate (IP3) receptors by reactive oxygen species. *Journal of Biological Chemistry* 289(12):8170-8181.
25. Agarwal A*, et al.* (2017) Transient opening of the mitochondrial permeability transition pore induces microdomain calcium transients in astrocyte processes. *Neuron* 93(3):587-605. e587.
26. Sherwood MW*, et al.* (2017) Astrocytic IP3Rs: Contribution to Ca2+ signalling and hippocampal LTP. *Glia* 65(3):502-513.
27. Petravicz J, Boyt KM, & McCarthy KD (2014) Astrocyte IP3R2-dependent Ca2+ signaling is not a major modulator of neuronal pathways governing behavior. *Front. Behav. Neurosci.* 8:384.

28. Srinivasan R, *et al.* (2015) Ca2+ signaling in astrocytes from Ip3r2-/-mice in brain slices and during startle responses in vivo. *Nat. Neurosci.* 18(5):708-717.
29. Sheppard CJR & Komphner R (1978) Resonant scanning optical microscope. *Appl. Opt.* 17(18):2879-2881.
30. Macias-Romero C, Zubkovs V, Wang S, & Roke S (2016) Wide-field medium-repetition-rate multiphoton microscopyreduces photodamage of living cells. *Biomed. Opt. Express* 7(4):1458-1467.
31. Liu Y, Sonek G, Berns M, & Tromberg B (1996) Physiological monitoring of optically trapped cells: assessing the effects of confinement by 1064-nm laser tweezers using microfluorometry. *Biophys. J.* 71(4):2158-2167.
32. Peterman EJ, Gittes F, & Schmidt CF (2003) Laser-induced heating in optical traps. *Biophys. J.* 84(2):1308-1316.
33. Kalmbach AS & Waters J (2012) Brain surface temperature under a craniotomy. *J. Neurophysiol.* 108(11):3138-3146.
34. Chen X, *et al.* (2012) LOTOS-based two-photon calcium imaging of dendritic spines in vivo. *Nat. Prot.* 7(10):1818.
35. Iyer V, Hoogland TM, & Saggau P (2006) Fast functional imaging of single neurons using random-access multiphoton (RAMP) microscopy. *J. Neurophysiol.* 95(1):535-545.
36. Salome R, *et al.* (2006) Ultrafast random-access scanning in two-photon microscopy using acousto-optic deflectors. *J. Neurosci. Meth.* 154(1-2):161-174.
37. Reddy GD, Kelleher K, Fink R, & Saggau P (2008) Three-dimensional random access multiphoton microscopy for functional imaging of neuronal activity. *Nat. Neurosci.* 11(6):713-720.
38. Icha J, Weber M, Waters JC, & Norden C (2017) Phototoxicity in live fluorescence microscopy, and how to avoid it. *Bioessays* 39(8).
39. Horton NG, *et al.* (2013) In vivo three-photon microscopy of subcortical structures within an intact mouse brain. *Nat. Photon.* 7(3):205.
40. Guesmi K, *et al.* (2018) Dual-color deep-tissue three-photon microscopy with a multiband infrared laser. *Light: Sci. Appl.* in press.
41. Nett WJ, Oloff SH, & Mccarthy KD (2002) Hippocampal astrocytes in situ exhibit calcium oscillations that occur independent of neuronal activity. *J. Neurophysiol.* 87(1):528-537.
42. Wang X, *et al.* (2006) Astrocytic Ca 2+ signaling evoked by sensory stimulation in vivo. *Nat. Neurosci.* 9(6):816.
43. Sun M-Y, *et al.* (2014) Astrocyte calcium microdomains are inhibited by Bafilomycin A1 and cannot be replicated by low-level Schaffer collateral stimulation in situ. *Cell Calcium* 55(1):1-16.
44. Xu H, *et al.* (2002) TRPV3 is a calcium-permeable temperature-sensitive cation channel. *Nature* 418(6894):181.
45. Xiao B, Coste B, Mathur J, & Patapoutian A (2011) Temperature-dependent STIM1 activation induces Ca2+ influx and modulates gene expression. *Nat. Chem. Biol.* 7(6):351-358.
46. Chowdhury S, Jarecki BW, & Chanda B (2014) A molecular framework for temperature-dependent gating of ion channels. *Cell* 158(5):1148-1158.
47. Shibasaki K, Ikenaka K, Tamalu F, Tominaga M, & Ishizaki Y (2014) A novel subtype of astrocytes expressing TRPV4 (transient receptor potential vanilloid 4) regulates neuronal excitability via release of gliotransmitters. *J. Cell Biol.* 289(21):14470-14480.

48. Gao X, Wu L, & O'Neil RG (2003) Temperature-modulated diversity of TRPV4 channel gating activation by physical stresses and phorbol ester derivatives through protein kinase C-dependent and-independent pathways. *J. Biol. Chem.* 278(29):27129-27137.
49. Kühn FJ, Heiner I, & Lückhoff A (2005) TRPM2: a calcium influx pathway regulated by oxidative stress and the novel second messenger ADP-ribose. *Pflügers Arch.* 451(1):212-219.
50. Xi P, Andegeko Y, Weisel LR, Lozovoy VV, & Dantus M (2008) Greater signal, increased depth, and less photobleaching in two-photon microscopy with 10 fs pulses. *Opt. Commun.* 281(7):1841-1849.
51. Pang S, Yeh AT, Wang C, & Meissner KE (2009) Beyond the 1/Tp limit: two-photon-excited fluorescence using pulses as short as sub-10-fs. *J. Biomd. Opt.* 14(5):054041.
52. Kawano H, *et al.* (2003) Attenuation of photobleaching in two-photon excitation fluorescence from green fluorescent protein with shaped excitation pulses. *Biochem. Biophys. Res. Commun.* 311(3):592-596.
53. Madisen L, *et al.* (2015) Transgenic mice for intersectional targeting of neural sensors and effectors with high specificity and performance. *Neuron* 85(5):942-958.
54. Slezak M, *et al.* (2007) Transgenic mice for conditional gene manipulation in astroglial cells. *Glia* 55(15):1565-1576.
55. Cesana E, *et al.* (2013) Granule cell ascending axon excitatory synapses onto Golgi cells implement a potent feedback circuit in the cerebellar granular layer. *J. Neurosci.* 33(30):12430-12446.
56. Ducros M, *et al.* (2011) Efficient large core fiber-based detection for multi-channel two-photon fluorescence microscopy and spectral unmixing. *J. Neurosci. Meth.* 198(2):172-180.
57. Oheim M, Beaurepaire E, Chaigneau E, Mertz J, & Charpak S (2001) Two-photon microscopy in brain tissue: parameters influencing the imaging depth. *J. Neurosci. Meth.* 111(1):29-37.
58. Schneider CA, Rasband WS, & Eliceiri KW (2012) NIH Image to ImageJ: 25 years of image analysis. *Nat. Meth.* 9(7):671.
59. Rueden CT, *et al.* (2017) ImageJ2: ImageJ for the next generation of scientific image data. *BMC bioinformatics* 18(1):529.
60. Schindelin J, *et al.* (2012) Fiji: an open-source platform for biological-image analysis. *Nat. Meth.* 9(7):676.
61. Bethge P, *et al.* (2017) An R-CaMP1. 07 reporter mouse for cell-type-specific expression of a sensitive red fluorescent calcium indicator. *PloS one* 12(6):e0179460.
62. Van Veen R, *et al.* (2005) Determination of visible near-IR absorption coefficients of mammalian fat using time-and spatially resolved diffuse reflectance and transmission spectroscopy. *J. Biomed. Opt.* 10(5):054004.
63. Chung S, *et al.* (2008) In vivo water state measurements in breast cancer using broadband diffuse optical spectroscopy. *Physics Med. Biol.* 53(23):6713.